land

MDPI

Article

Quantifying Evapotranspiration and Environmental Factors in the Abandoned Saline Farmland Using Landsat Archives

Liya Zhao [1,2], Jingwei Wu [1,*], Qi Yang [3], Hang Zhao [1], Jun Mao [1], Ziyang Yu [2,4], Yanqi Liu [2] and Anne Gobin [2,*]

[1] State Key Laboratory of Water Resources and Hydropower Engineering Sciences, Wuhan University, Wuhan 430072, China; zhaoliya921@whu.edu.cn (L.Z.); m15663583512@163.com (H.Z.); maojun@whu.edu.cn (J.M.)
[2] Division of Soil and Water Management, Department of Earth and Environmental Sciences, KU Leuven, 3001 Leuven, Belgium; ziyangyu@yeah.net (Z.Y.); yanqi.liu@kuleuven.be (Y.L.)
[3] Department of Biogeochemical Integration, Max Planck Institute for Biogeochemistry, 07745 Jena, Germany; qiyang@bgc-jena.mpg.de
[4] School of Humanities and Law, Northeastern University, Shenyang 110169, China
* Correspondence: jingwei.wu@whu.edu.cn (J.W.); anne.gobin@kuleuven.be (A.G.)

Abstract: This study investigates the complex interaction of biophysical and meteorological factors that drive evapotranspiration (ET) in saline environments. Leveraging a total of 182 cloud-free Landsat 5/8 time-series data from 1988 to 2019, we employed the Surface Energy Balance System (SEBS) model to quantify ET and investigate its relationships with soil salinity, vegetation cover, groundwater depth, and landscape metrics. We validated the predicted ET at two experimental sites using ET observation calculated by a water balance model. The result shows an R^2 of 0.78 and RMSE of 0.91 mm for the SEBS predicted ET, indicating high accuracy of the ET estimation. We detected abandoned saline farmland patches across Hetao and extracted the normalized difference vegetation index (NDVI), salinization index (SI), and the predicted ET for analysis. The results indicate that ET is negatively correlated with SI with a Pearson correlation coefficient (r) up to −0.7, while ET is positively correlated with NDVI (r = 0.4). In addition, we designed a control-variable experiment in the Yichang subdistrict to investigate the effects of groundwater depth, land aggregation index, soil salinity index, and the area of abandoned saline farmland patches on ET. The results indicate that increased NDVI could significantly enhance ET, while smaller saline farmland patches exhibited greater sensitivity to groundwater recharge, with higher averaged ET than larger patches. Moreover, we analyzed factor importance using Lasso regression and Random Forest (RF) regression. The result shows that the ranking of the importance of the features is consistent for both methods and for all the features, with NDVI being the most important (with an RF importance score of 0.4), followed by groundwater table depth (GWTD), and the influence of the surface area of abandoned saline farmland being the weakest. We found that smaller patches of abandoned saline farmland were more sensitive to changes in groundwater levels induced by nearby irrigation, affecting their averaged ET more dynamically than larger patches. Decreasing patch size over time indicates ongoing changes in land management and ecological conditions. This study, through a multifactor analysis of ET in abandoned saline farmland and its intrinsic factors, provides a reference for evaluating the dry drainage efficiency of abandoned saline farmland in a dry drainage system.

Keywords: evapotranspiration; abandoned saline farmland; Hetao Irrigation District; Landsat; soil salinity; vegetation cover; aggregation index; dry drainage system

Academic Editors: Tiago Brito Ramos, Maria da Conceição Gonçalves and Mohammad Farzamian

Received: 26 November 2024
Revised: 22 January 2025
Accepted: 27 January 2025
Published: 30 January 2025

Citation: Zhao, L.; Wu, J.; Yang, Q.; Zhao, H.; Mao, J.; Yu, Z.; Liu, Y.; Gobin, A. Quantifying Evapotranspiration and Environmental Factors in the Abandoned Saline Farmland Using Landsat Archives. *Land* **2025**, *14*, 283. https://doi.org/10.3390/land14020283

1. Introduction

In arid and semi-arid regions with shallow groundwater tables, secondary salinization induced by human/land interactions is a prominent process of agricultural land degradation [1–3]. As soil salinization increases, the salinity level of the soil in salinized farmland may exceed the salt tolerance of crops, rendering the land unsuitable for agricultural use if no interventions are made [4,5]. This kind of saline area is called abandoned saline farmland (Figure 1). Many such abandoned saline farmland may emerge in large irrigation districts with shallow groundwater levels in arid and semi-arid regions [6].

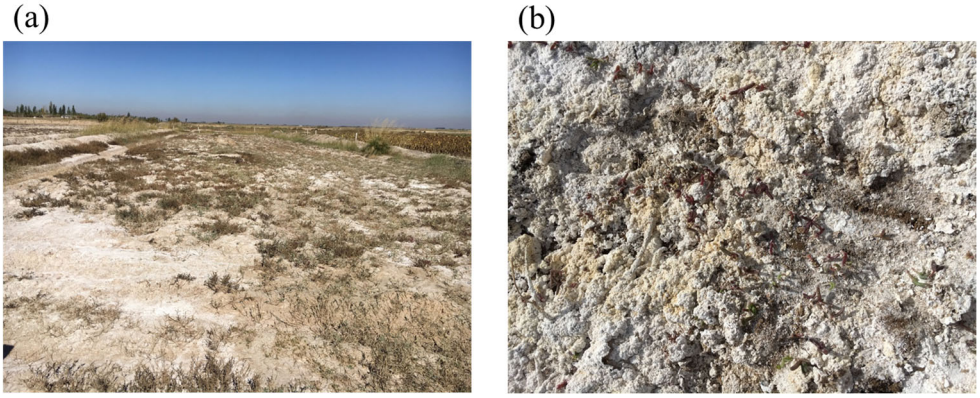

Figure 1. Abandoned saline farmland (**a**) and its surface (**b**), photographed in the Hetao Irrigation District of Inner Mongolia, China.

In a landscape configuration comprising both abandoned saline farmland and farmland (Figure 2), the groundwater table in abandoned saline farmland is often lower than that in surrounding farmland. This results in soil moisture from the farmland converging toward the abandoned saline farmland, forming a dry drainage system [7–9]. Abandoned saline farmlands act as evaporation sinks, receiving water and salts from adjacent farmlands, thereby playing a crucial role in sustainable agriculture. In such dry drainage systems, evapotranspiration (ET) from abandoned saline farmland serves as a critical driving force, directly determining their capacity for salt drainage.

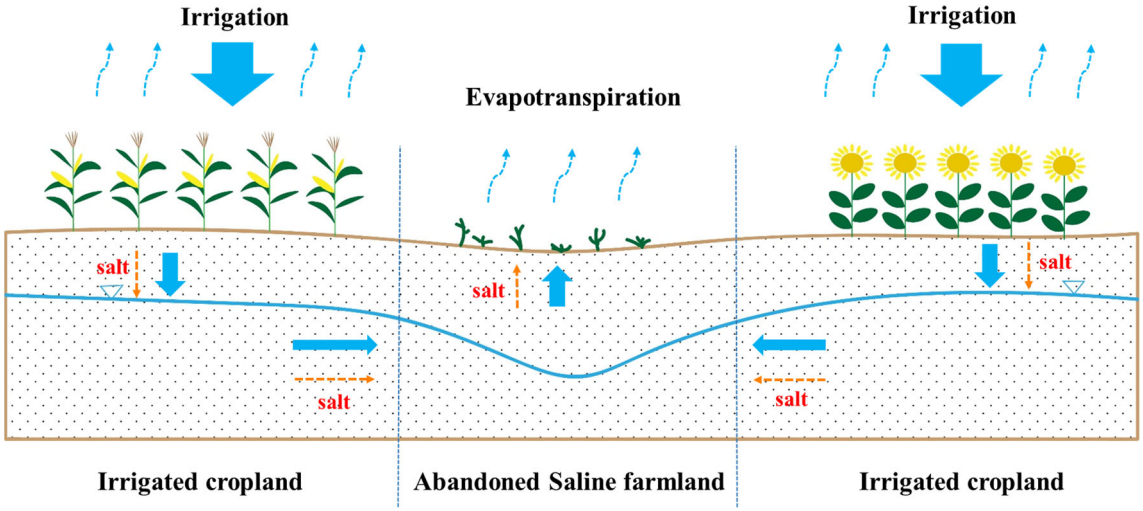

Figure 2. Schematic diagram of a dry drainage system, where the abandoned farmland acts as an evaporation sink with a lower groundwater table. The groundwater and dissolved salts move from the surrounding crop field to the abandoned farmland, which provides a natural-based solution for sustainable farming.

Previous studies investigated dry drainage systems and the factors influencing the salt drainage capacity of abandoned saline farmland. In California's San Joaquin Valley, a higher ratio of cultivated-to-abandoned land gradually decreased the effectiveness of dry salt drainage [10]. However, when the elevation difference of abandoned land exceeded 0.3 m, this decrease became less prominent. Additionally, when the cultivated-to-abandoned land ratio was below 2, the drainage needs of cultivated land were generally met. In the Indus River Basin of Pakistan, the cultivated-to-abandoned land ratio required to maintain salt balance increased from 0.83 to 1.60 as the groundwater depth decreased from 2.0 m to 1.0 m [7]. However, considering the needs of crop growth and soil leaching, the optimal groundwater depth should be below 1.5 m, and the cultivated-to-abandoned land ratio should be around 1 [7,11]. These studies indicate that in arid or semi-arid regions, rational allocation of cultivated and abandoned land, coupled with the use of natural or artificial lowlands for dry salt drainage, can effectively maintain the water/salt balance of cultivated land, mitigate the hazards of salinization, reduce the impact on the surrounding ecological environment, and promote the sustainable development of irrigated agriculture.

Previous studies on dry salt drainage systems have mostly focused on the size and spatial distribution of abandoned saline farmland, neglecting surface characteristics such as vegetation cover and surface salinization. ET drives the functioning of dry salt drainage systems and can be used as an indicator to evaluate their effectiveness. Therefore, this study uses the ET of abandoned saline farmland as the evaluation indicator to assess its dry salt drainage capacity and to analyze the influence of various factors on its dry drainage function.

Whether in dry salt drainage systems or in regular agricultural water cycling systems, ET plays a critical role in the water, energy, and soil cycles by facilitating the transfer of water from the land surface to the atmosphere, significantly influencing soil moisture, groundwater recharge, and local climatic conditions. In the agricultural context, ET determines crop water requirements, affects irrigation efficiency, and helps maintain soil salinity balance, thereby contributing to sustainable agricultural practices [12]. In addition, ET is a key driver in the surface energy balance, regulating energy exchange processes and influencing ecosystem functioning. Studies highlight the need for accurate ET quantification to optimize water resource management and address environmental challenges in arid and semi-arid regions, where water scarcity and salinity pose considerable risks to agricultural sustainability [13–18]. Accurate quantification of land surface ET is paramount for optimizing agricultural practices such as irrigation and planting, managing groundwater resources, and modeling hydrological processes [19], all of which are necessary to manage saline regions. The application of remote sensing technology, with its spatiotemporal data advantages, enables effective monitoring of ET in abandoned saline farmland. Optical and microwave remote sensing data facilitate the analysis of factors influencing the ET potential of abandoned saline farmland, such as soil salinization, vegetation greenness, patch area, spatial configuration, and groundwater table depth [20–24].

Methods for remote sensing-based estimation of ET can be broadly categorized into three types: (1) the crop coefficient method based on reference crop evapotranspiration (ET_0) [25], (2) the surface conductance method relying on the Penman–Monteith equation [26], and (3) the land surface temperature (LST)-based approach [27]. The first method is relatively straightforward, requiring only meteorological data and empirical crop coefficients to calculate actual ET. However, accurately estimating crop coefficients at the regional level is often challenging due to their dependence on crop varieties, growth stages, and fertilization practices [28]. The accuracy of the second method hinges on precise surface conductance estimation, which relates to stomatal conductance, scales up to the canopy level, and is linked not only to leaf photosynthetic capacity and canopy structure but also

to soil characteristics [29]. Empirical methods employing the Jarvis formula are commonly used for remote sensing based on estimating surface conductance [30]. Due to current gaps in the understanding of vegetation/water/carbon interactions, vertical light use (light regime), and the spatial distribution of atmospheric carbon dioxide, non-empirical estimation of surface conductance at the regional scale remains challenging.

The LST-based method relies on remote sensing observations and has gained popularity for estimating regional ET [22,31,32]. There are two theoretical approaches: the feature space method and the energy balance method. The feature space method assumes that the scatter plot of LST and vegetation index (e.g., NDVI) forms a distinctive triangular or trapezoidal feature space. The upper boundary of this feature space is referred to as the dry edge, indicating that crops are experiencing water stress, resulting in stomatal closure and the highest canopy temperature. In contrast, the lower boundary of the feature space is known as the wet edge and represents potential evaporation. Consequently, actual ET can be calculated based on potential evaporation and the distance between the LST and the dry and wet edges [20]. In contrast, the energy balance method calculates various energy components (net radiation and sensible heat flux) to estimate ET (latent heat flux) by using the land surface energy balance equation, making it a more theoretically based approach.

When estimating land surface ET using remote sensing data, there is a higher degree of uncertainty and complexity in estimating ET for saline agricultural land and abandoned saline farmland than for non-saline agricultural land [33,34]. In particular, an increase in soil salinity results in higher soil matric suction, while excessive salinity can lead to soil compaction, reducing the soil's ability to conduct water. In addition, during the spring season, the return of salt (crystallization) in saline agricultural land and abandoned saline farmland increases the albedo of the land surface, which affects the energy balance [35]. In the Hetao Irrigation District, existing literature often relies on a relatively simple crop coefficient method to estimate ET and often lacks an analysis of how the degree of salinization, planting patterns, and spatial distribution of abandoned saline farmland affect ET. This study integrates the spatial structure information of abandoned saline farmland in the Hetao Irrigation District and employs the Surface Energy Balance System (SEBS) model to estimate ET in these areas. By analyzing the effects of different salinization levels and vegetation coverage on ET, the study reveals the relationships between abandoned saline farmland ET and factors such as salinity and vegetation conditions. Additionally, ecological landscape indices are utilized to explore the interactions between the spatial configuration of abandoned saline farmland and ET, further enhancing the understanding and predictive capability of abandoned saline farmland ET processes. The aim is to provide a reference for evaluating the drainage efficiency of the abandoned saline farmland in the dry drainage system.

2. Methodology

2.1. Study Area

The Hetao Irrigation District, located in the Inner Mongolia Autonomous Region of China (40.1°–41.4° N, 106.1°–109.4° E) (Figure 3a), is an important agricultural area. Situated along the southern edge of the Yellow River, its unique geographical position and topography turn the Hetao Irrigation District into an oasis in the middle of the desert. The Hetao Irrigation District is characterized by a typical arid and semi-arid climate with low precipitation, high evaporation, and abundant sunshine. According to meteorological records from 1999 to 2013 (http://data.cma.cn, accessed on 26 December 2024), the mean annual temperature is 8.2 °C. Winter temperatures are relatively low, with a prolonged period of soil freezing lasting up to 180 days from November to April, and a maximum frozen soil depth of 1.32 m. July is the hottest month, with an average temperature of

24.62 °C. The mean annual precipitation is only 180 mm, 89% of which is concentrated between May and September, with the highest monthly precipitation of 41 mm occurring in July. Evaporation significantly exceeds precipitation, with a mean annual pan evaporation of 2176 mm, peaking at 347.3 mm in May. Summer has the longest sunshine duration, exceeding 10 h per day, while winter has the shortest, with around 6 h per day.

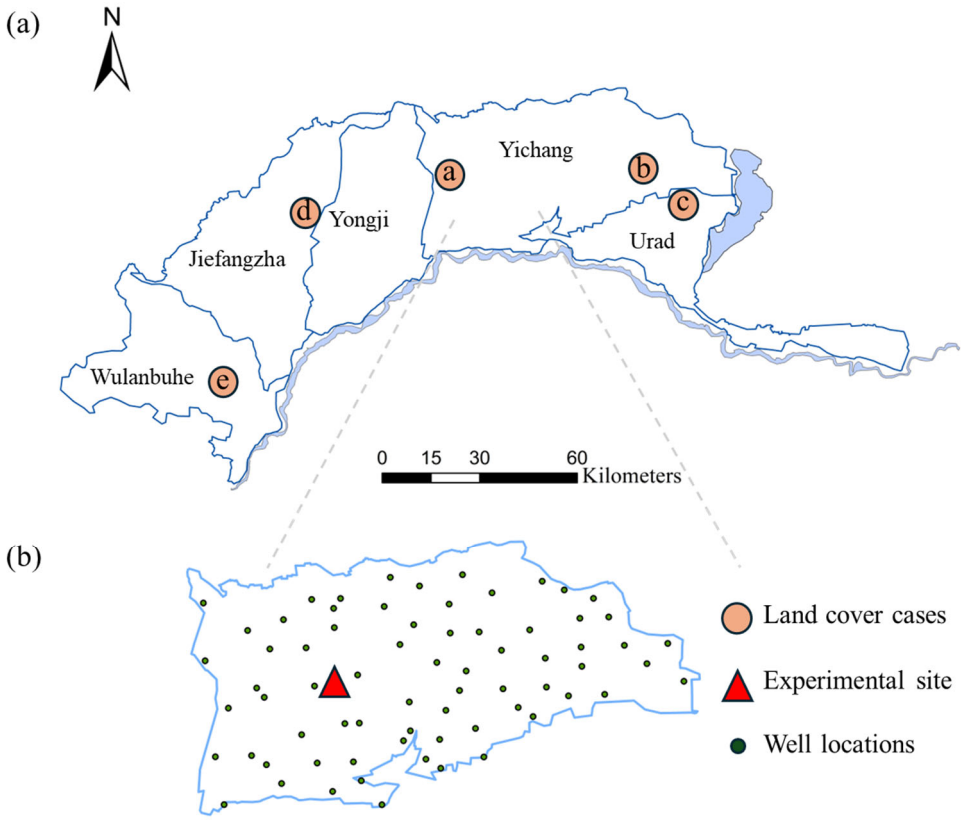

Figure 3. Location of land cover cases and five sub-irrigation districts of the Hetao Irrigation District (**a**); Location of the experimental site and well locations of the Yichang subdistrict (**b**).

The high evaporative demand and limited precipitation make agriculture highly dependent on irrigation while exacerbating the risk of soil salinization. In 2023, the agricultural water consumption in the Hetao Irrigation District was 4.21 billion m^3. Irrigation water is mainly sourced from the Yellow River, with a small amount from groundwater in well-irrigated areas (https://www.stats.gov.cn/sj/ndsj/, accessed on 26 December 2024). The soil is predominantly alluvial with a silt/loam texture. The Hetao Irrigation District is predominantly composed of agricultural lands, with spring wheat, maize, and sunflower being the main crops. Beyond the agricultural fields, the landscape includes woodlands, grasslands, sand dunes, lakes, residential areas, and saline wastelands. The saline wastelands, with a total area of approximately 190 km^2 in 2019 [5], are interspersed throughout the agricultural areas. While some of these wastelands are barren and devoid of vegetation, others support halophytic plants such as tamarisk (*Tamarix*), alkali grass (*Puccinellia*), and reed grass (*Phragmites*) [36]. Due to high evaporation, low precipitation, and shallow groundwater levels, the Hetao Irrigation District is highly susceptible to secondary salinization. Research has shown that most areas are currently characterized by mild or no salinization in the Hetao Irrigation District; certain regions exhibit high levels of salinization, typically identified as abandoned saline farmlands. In the subsequent analysis, these regions are referred to as "patches".

The impact of abandoned saline farmland patches on ET was analyzed using five land cover cases, each covering 5765 ha in four different sub-irrigation districts located in the Hetao Irrigation District. These cases were selected based on the maps in Figure 3, ensuring that there was sufficient distance between them. The land cover of the five cases is shown in Figure 4a–e and is based on the land cover classification results from [5], with the location of the five cases shown in Figure 3a. For the land cover map, a total of 150 verification points were used to assess the performance of the land cover classification and, in particular, the detection of abandoned farmland [5]. All evaluation metrics exceeded 0.70, indicating satisfactory accuracy. Exceptional results were obtained for wheat and water bodies, with metrics exceeding 0.93, closely followed by high metrics for abandoned farmland and other crops. Similar to [37,38], the distinctive VI time series facilitated the classification of these classes. In contrast, residential areas were frequently misclassified due to their complex composition and high spatial variability. Overall, the land cover map achieved a robust performance, with a kappa coefficient of 0.876.

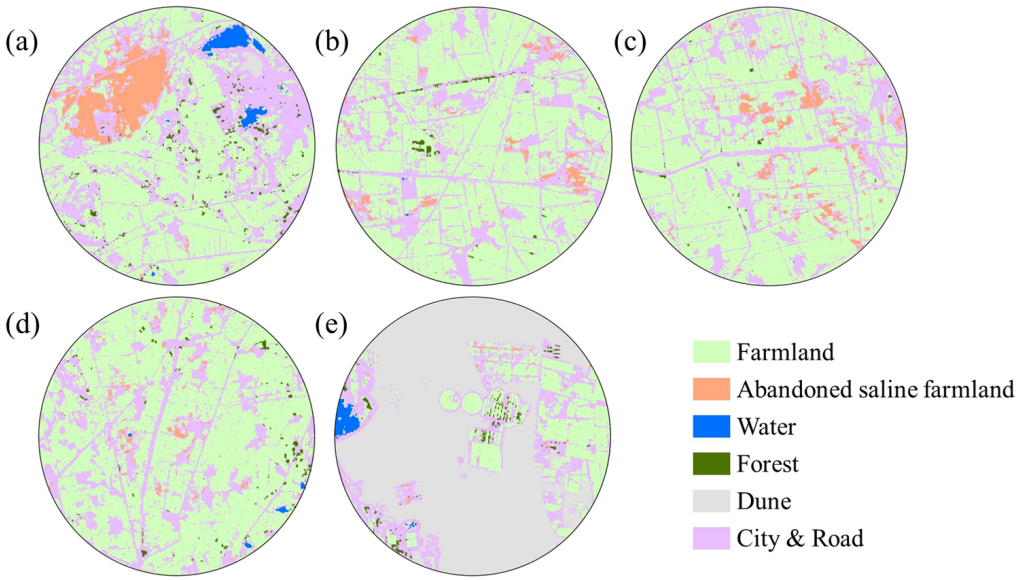

Figure 4. Land cover of five cases with a surface area of 5765 ha. The location of the cases is shown in Figure 3a, where (**a**) Case in Yichang sub-irrigation district, (**b**) Case in Yichang sub-irrigation district, (**c**) Case in Urat sub-irrigation district, (**d**) Case in Jiefangzha sub-irrigation district, and (**e**) Case in Wulanbuhe sub-irrigation district.

2.2. Data Processing

Vegetation coverage (fc), Normalized Difference Vegetation Index (NDVI), and LST were derived from the Landsat satellite imagery (Landsat-5 TM and Landsat-8 OLI/TIRS), downloaded from the United States Geological Survey (USGS) (https://earthexplorer.usgs.gov/, accessed on 26 December 2024). The area of interest was the Hetao Irrigation District, and both level-1 and level-2 were acquired for the selected period. Level-1 data were used to calculate brightness temperature for LST, while level-2 surface reflectance data, already radiometrically calibrated, were used to estimate surface reflectance, NDVI, and SI. To ensure good data quality, we only selected Landsat satellite imageries with cloud cover of less than 20% to download. The date information is in Supplementary Table S1.

2.2.1. Vegetation Density

Vegetation cover is determined using the following empirical formula, which relies on the NDVI for calculation [39].

$$f_c = \frac{NDVI - NDVI_{min}}{NDVI_{max} - NDVI_{min}} \tag{1}$$

where $NDVI_{min}$ and $NDVI_{max}$ are the upper and lower limits of $NDVI$.

In this study $NDVI_{min} = 0.05$ and $NDVI_{max} = 0.7$. If $NDVI > NDVI_{max}$, $f_c = 1$; if $NDVI < NDVI_{min}$, $f_c = 0$.

2.2.2. Surface Emissivity

The surface emissivity ε is determined using the equation provided by Qin [39].

$$\varepsilon = f_c R_v \varepsilon_v + (1 - P_v) R_s \varepsilon_s + d\varepsilon \tag{2}$$

$$R_v = 0.9332 + 0.0585 NDVI \tag{3}$$

$$R_s = 0.9902 + 0.106 NDVI \tag{4}$$

$$d\varepsilon = \begin{cases} 0.0038 f_c, & f_c \leq 0.5 \\ 0.0038(1 - f_c), & f_c > 0.5 \\ 0.0019, & f_c = 0.5 \end{cases} \tag{5}$$

where R_v and R_s are the temperature ratios of vegetation and bare soil, ε_v and ε_s represent the emissivity of vegetation and bare soil in the TM6 band interval. $d\varepsilon$ corresponds to the gradient component of the surface emissivity and is calculated using Equation (5).

2.2.3. Land Surface Temperature

The brightness temperature is derived from Landsat's level-1 data using ENVI 5.3 software. The calculation of land surface temperature (LST) is accomplished using a single-window algorithm [40]. This algorithm relies on the thermal radiative transfer equation and offers a straightforward and efficient approach to computing LST using only one of the Landsat thermal bands.

$$T_s = \frac{\{a(1 - C - D) + [b(1 - C - D) + C + D]T_b - DT_a\}}{C_6} \tag{6}$$

$$C = \varepsilon \cdot \tau \tag{7}$$

$$D = (1 - \tau)[1 + (1 - \varepsilon)\tau] \tag{8}$$

where T_a is the effective mean atmospheric temperature, T_b is the brightness temperature, τ is the atmospheric transmittance, a and b are reference coefficients. When the surface temperature ranges from 0 °C to 70 °C, $a = 67.355351$, $b = 0.458606$.

2.3. Evapotranspiration Calculation

2.3.1. The Instantaneous Evapotranspiration Calculation

The Surface Energy Balance System (SEBS) model was selected because of its ability to estimate spatially distributed ET using remote sensing data. Unlike empirical models, SEBS is based on physical principles and calculates ET as the residual of surface energy fluxes [41]. Its integration with satellite-derived parameters, such as surface temperature and albedo, allows for reliable ET estimates across heterogeneous landscapes, including abandoned saline farmland. Compared to the Penman–Monteith method, which requires extensive ground-based inputs, SEBS provides a scalable solution for regional studies by using

satellite data [42]. Furthermore, the model's ability to account for atmospheric stability makes it particularly suitable for semi-arid and saline environments where ET dynamics are complex. The 16-day temporal resolution of the Landsat archive, coupled with frequent cloud cover, can limit the ability to capture short-term intra-seasonal variations in ET. In addition, the SEBS model relies on assumptions of surface homogeneity and atmospheric similarity. Despite these limitations, the advantages of using Landsat data for ET estimation generally outweigh the disadvantages.

The SEBS model is a computational framework for estimating ET using a single-source energy balance approach. Its key strength lies in its ability to effectively differentiate the roughness variations in heat and momentum transfer between the vegetation canopy and Earth's surface by introducing the concept of residual resistance. The SEBS model comprises four primary modules: (1) retrieval of surface physical parameters using remote sensing data, (2) estimation of the roughness length for heat transfer, (3) calculation of sensible heat flux, and (4) calculation of latent heat flux. SEBS, based on the energy balance of Earth's surface, can be expressed by the following equation:

$$R_n = G_0 + H + \lambda E \tag{9}$$

where R_n is net radiation, G_0 is soil heat flux, H is sensible heat flux, λE represents the latent heat flux, λ is the latent heat of vaporization, and E is the actual ET.

The R_n is calculated as:

$$R_n = (1 - \alpha) \cdot R_{swd} + \varepsilon \cdot R_{lwd} - \varepsilon \cdot \sigma \cdot T_0^4 \tag{10}$$

where α is the surface albedo, R_{swd} and R_{lwd} are the downward shortwave and downward longwave radiation, respectively, ε is the surface emissivity, T_0 is the surface temperature, and σ is the Stefan–Boltzmann constant, which has a value of 5.670367×10^{-8} $W \cdot m^{-2} \cdot K^{-4}$.

The G_0 is calculated as follows,

$$G_0 = R_n . [\Gamma_c + (1 - f_c) . (\Gamma_s - \Gamma_c)] \tag{11}$$

where Γ_c is the relationship between soil heat flux and net radiation in the presence of vegetation and Γ_s is the relationship between soil heat flux and net radiation in bare soil; when f_c equals 0, Γ_s equals 0.315; conversely, when f_c equals 1, Γ_s equals 0.05.

The instantaneous ET is calculated using the ET fraction-based method,

$$\Lambda_r = 1 - \frac{H - H_{wet}}{H_{dry} - H_{wet}} \tag{12}$$

$$\lambda E = \Lambda_r \lambda E_{wet} \tag{13}$$

where Λ_r is the ET fraction. H_{wet} and H_{dry} are the dry and wet limits of H. λE is the actual ET.

2.3.2. Daily and Monthly Evapotranspiration Calculation

We upscale the instantaneous ET to a daily scale by assuming that the $ET/(R_n - G)$ fraction is a constant throughout the day. As a result, the daily ET can be calculated as follows,

$$E = \frac{(\Lambda \times R_{nd})}{\lambda} \tag{14}$$

Due to the absence of daily Landsat imagery, monthly scale ET is derived by using the Penman–Monteith formula [26] to calculate the potential ET pattern. The calculation model inversely estimates the potential ET for a given day and calculates the ratio between

the potential ET values for each day of the month. Using these ratio coefficients, the ET for each day of the month is determined sequentially and then summed cumulatively to obtain the monthly ET. The ET values from April to October can be obtained by adding up the ET value for the non-freezing period (April to October).

2.3.3. Evapotranspiration Validation

The root zone water balance model [43] was used to validate the ET calculation results. This model takes into account the effects of groundwater leakage and recharge. By applying the root zone water balance, the ET amount can be calculated as follows:

$$ET_i = W_i - W_{i-1} + P_i + I_i + CR_i - DP_i \quad (15)$$

where i is the day number, W_i is the soil moisture content in the root zone, W_{i-1} is the soil moisture content on the previous day, P_i represents the effective rainfall, I_i is the irrigation, CR_i is the groundwater recharge, DP_i is the root zone percolation. The calculation detail for each component in Equation (15) can be found in [43].

To validate the ET results derived from remote sensing, two experimental sites in the Hetao Irrigation District (Figure 3b) were selected in 2019. One site is a fallow field, and the other site is a sunflower field. The experiments included data collection on groundwater table levels, soil moisture content, precipitation, and irrigation. Daily ET was calculated using a water balance model, and the results were compared with the ET calculated from remote sensing in 2019 for analysis. Soil moisture content was monitored using Hydra soil moisture sensors, with sampling depths of up to 1.4 m. The depth intervals were configured as follows: 0 cm–10 cm, 10 cm–30 cm, 30 cm–50 cm, 50 cm–70 cm, 70 cm–100 cm, and 100 cm–140 cm, with one sensor installed at each depth, resulting in a total of six sensors per sampling site (Figure 3b). With two sampling sites, a total of 12 monitoring sensors were installed. At each sampling site, groundwater levels were measured using wells equipped with HOBO water level loggers. Data were collected at daily intervals, and daily averages were recorded.

2.4. Abandoned Saline Farmland Spatial Information

The extraction of abandoned saline farmland (Figure 5) is based on the method developed by Zhao et al. [5]. Based on the idea of "elimination" to detect abandoned saline land step by step, more details can be found in [5].

This study uses the vector files of abandoned saline farmland and the ET values calculated for the non-freezing period. By extracting the ET values corresponding to each saline farmland patch using the boundary files, the ET values for each patch representing the unit-area ET of each abandoned saline farmland patch were obtained. This serves as the data foundation for analyzing the influence of various factors on the ET of abandoned saline farmland. In the analysis of influencing factors, the ET refers to the unit-area ET of abandoned saline farmland.

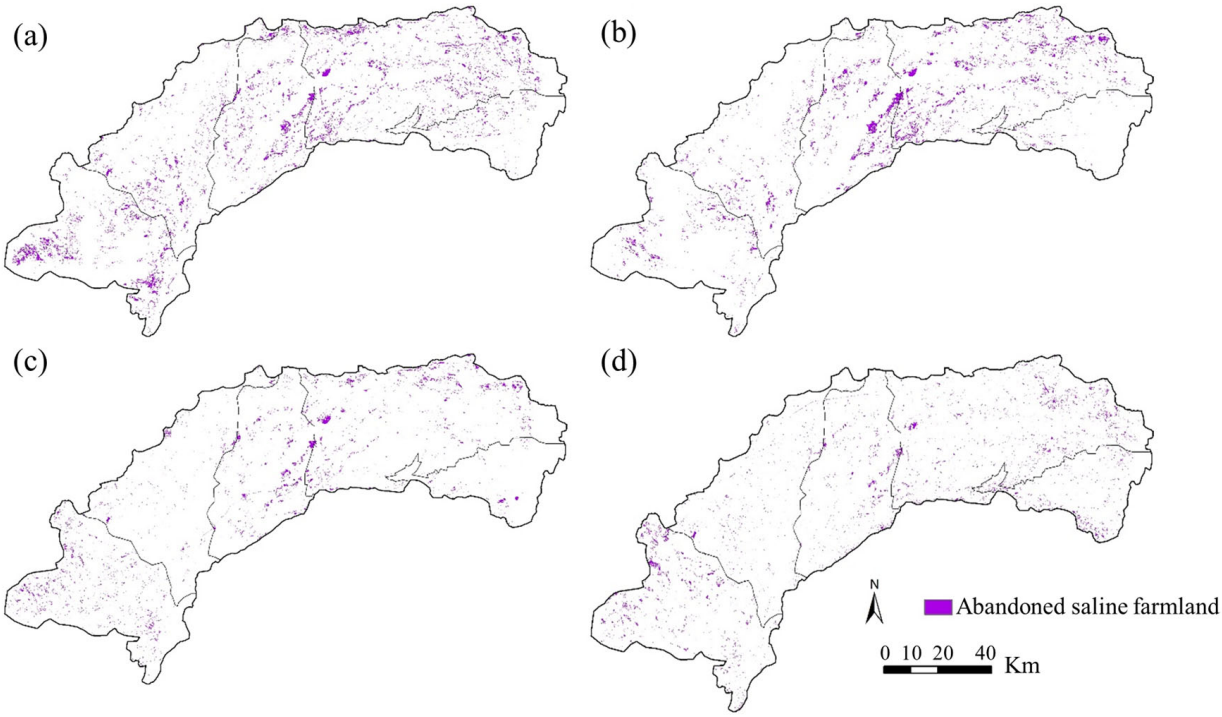

Figure 5. Distribution of abandoned saline farmland in the Hetao Irrigation District, (**a**) 1988, (**b**) 1998, (**c**) 2008, (**d**) 2018.

2.5. Factors Influencing Evapotranspiration

2.5.1. The Characteristic Index of Influencing Factors

To investigate the effects of vegetation, soil salinity, groundwater, and landscape layout on ET, we selected various indicators to represent these influences and quantify the effects of multiple factors on ET. Groundwater table depth (GWTD) and the area size of abandoned saline farmland are directly derived from observations. The GWTD was measured every five days. Vegetation coverage of abandoned saline farmland is represented using NDVI, the salinization level is characterized by the Salinization Index (SI), and spatial structure is described using the Aggregation Index (AI). A detailed introduction to SI and AI is provided below.

Salinization Index

In previous studies, the analysis of the effect of salinization on ET mostly involved measuring ET at different salinity levels and then analyzing its variation [44]. A systematic analysis was conducted using remote sensing methods, and the SI was used to represent the degree of salinization in the region. Applying the conversion formula for SI and soil salinity could achieve the conversion between SI and soil salinity, and more details can be found in [5].

$$SI = \sqrt{\rho_{blue} \cdot \rho_{red}} \tag{16}$$

where ρ_{blue} is the surface reflectance of blue band, ρ_{red} is the surface reflectance of red band.

The SI was validated against measurements of electrical conductivity (EC). Soil samples (0–5 cm depth) were collected at 33 sites (133 samples) from May 2018 to October 2019 [5]. Sampling coordinates were recorded using a GPS with ±1.45 m accuracy. A strong exponential relationship between SI and EC was derived (EC = 0.94 exp(10.51 SI) − 1.20) [5], enabling salinity classification into 0–4 dS/m (slight/no salinity), 4–8 dS/m (moderate), 8–16 dS/m (high), and >16 dS/m (extreme). Pixel counts per salinity class were used for

area estimation. Only cloud-free March–April imagery was used for salinity classification to avoid cropping effects.

Aggregation Index

We use landscape indices commonly used in landscape ecology to analyze the spatial configuration information of abandoned saline farmland for quantitative research. These landscape indices are examined at three different scales: patch scale (individual patches), patch type scale (combinations of several individual patches forming patch types), and landscape scale (the overall composition of different patch types in the landscape). Some frequently used landscape indices include the Patch Shape Index and the Landscape Aggregation Index.

The general mathematical expression for the Landscape Aggregation Index C [45] is as follows:

$$\mathrm{C} = C_{max} + \sum_{i=1}^{n}\sum_{j=1}^{n} P_{ij}\ln\left(P_{ij}\right) \tag{17}$$

where C_{max} is the maximum value of the aggregation index ($2\ln(n)$), n is the total number of patch types in the landscape, and P_{ij} is the probability of the patch types, i and j are adjacent. In a gridded landscape, P_{ij} is generally calculated as:

$$P_{ij} = P_i P_{\frac{j}{i}} \tag{18}$$

where P_i is the probability that a randomly selected grid cell belongs to patch type i (estimated by the area proportion of patch type i in the entire landscape), and $P_{j/i}$ is the conditional probability that patch type j is adjacent to i,

$$P_{\frac{j}{i}} = \frac{m_{ij}}{m_i} \tag{19}$$

where m_{ij} is the number of grid sides where patches i and j are adjacent, and m_i is the total number of sites for patch type i. When comparing different landscapes, the relative aggregation index C' is more appropriate and calculated as:

$$\mathrm{C}' = \frac{\mathrm{C}}{C_{max}} = 1 + \frac{\sum_{i=1}^{n}\sum_{j=1}^{n} P_{ij}\ln\left(P_{ij}\right)}{2\ln(n)} \tag{20}$$

AI [46] is an indicator based on the length of the ordinary boundaries between pixels of the same patch type. It can be calculated at both the class and landscape levels. AI ranges from 0 to 1, with 0 representing the lowest aggregation and 1 representing the highest aggregation. AI can be used to assess the degree of aggregation of different landscape types and their relationships to ecological processes.

$$AI = \left[\frac{g_{ii}}{max \rightarrow g_{ii}}\right] \tag{21}$$

where g_{ii} is the number of similar adjacent patches of the corresponding landscape type.

AI has several advantages in quantifying landscape spatial patterns. It is category-specific and independent of landscape composition, making it more accurate than other indices that measure overall landscape aggregation. Therefore, in this study, AI is used as an aggregation indicator for abandoned saline farmland.

2.5.2. Lasso Multivariate Regression Analysis

Lasso regression (Least Absolute Shrinkage and Selection Operator regression), commonly used in statistics and machine learning, is a regression analysis method that improves upon traditional multivariate linear regression by adding a penalty term to the loss function [47]. This penalty term is the sum of the absolute values of the coefficients and aims to impose certain constraints on the model to prevent overfitting and potentially reduce some regression coefficients to zero. As a result, Lasso regression predicts data and performs feature selection, automatically filtering out variables that significantly affect the target variable. The main difference between Lasso regression and ordinary multivariate regression (Ordinary Least Squares, OLS) lies in the coefficient constraints. Ordinary multivariate regression aims to minimize the sum of squares of the residuals with no direct restrictions on the size of the coefficients. In contrast, Lasso regression introduces an L1 penalty (the sum of the absolute values of the coefficients) to limit the size of the coefficients, which may result in some coefficients becoming zero, thereby achieving variable selection and dimensionality reduction. The cost function of the Lasso regression is shown in the following formula:

$$Loss = \frac{1}{n}\sum_{i=1}^{n}\left(y_i - \sum_{j-1}^{p} x_{ij}\beta_j\right)^2 + \lambda\sum_{j-1}^{p}|\beta_j| \quad (22)$$

where n is the number of samples; p is the number of features (or predictor variables); y_i is the response variable for the i-th observation; x_{ij} is the j-th feature of the i-th observation; β_j is the coefficient of the j-th feature; λ is the regularization parameter that controls the strength of the penalty term.

Lasso regression is particularly effective in dealing with datasets that have multicollinearity or more features than samples. Therefore, Lasso regression is superior to ordinary multivariate regression in terms of feature selection and handling high-dimensional data. Feature importance analysis is performed using the regression coefficients obtained from the Lasso regression as the importance indices for each feature. The input data are first standardized to eliminate scale differences between the inputs before performing Lasso regression analysis.

2.5.3. Feature Importance Analysis Based on Random Forest

Random Forest (RF) is an ensemble learning method that makes predictions by constructing multiple decision trees and aggregating their results [48]. Each decision tree is trained on a random subset of the dataset during the RF training process. Suppose a particular input feature is frequently used in the decision trees of RF to partition data and significantly reduce Gini impurity. In this case, this feature is considered essential.

$$G(S) = \sum_{k=1}^{c} p_k(1 - p_k) \quad (23)$$

where $G(S)$ represents the Gini impurity and p_k is the selection probability for each decision tree.

Feature importance in Random Forests is typically determined by calculating the average reduction in impurity (Mean Decrease in Impurity, MDI) for each feature across all the trees.

$$\Delta G = G(parent) - \left(\frac{N_{left}}{N_{parent}}G(left) + \frac{N_{right}}{N_{parent}}G(right)\right) \quad (24)$$

where ΔI represents the average reduction in Gini impurity, $G(parent)$, $G(left)$, and $G(right)$ are the impurities of the parent node, left child node, and right child node, respectively. N_{parent}, N_{left}, and N_{right} are the number of samples in the respective nodes.

2.5.4. Shapley Feature Importance Analysis Method

The Shapley feature importance analysis method, which originated from cooperative game theory [49], is a technique for evaluating and interpreting machine learning models. In recent years, this method has been widely applied to quantify and explain the contribution of each feature in machine learning models to the prediction results. Its principle is based on cooperative game theory, considering all possible combinations of features and calculating the impact on model predictions when a particular feature is added or removed from these combinations. The advantage of this method is that it provides a comprehensive and balanced perspective on the importance of features, ensuring that the evaluation of feature contributions is neither biased toward frequently occurring features nor toward rare features. The calculation process of the Shapley method is as follows:

$$f(x) = g(x') = \phi_0 + \sum_{i=1}^{M} \phi_i x' \tag{25}$$

where f(x) is the model to be evaluated; g(x) is the explanatory model; $x = h_x(x')$, $x \in \{0,1\}^M$; M represents the number of input features; ϕ_i is the feature contribution of feature i (i.e., the Shapley value). The explanatory model g(x) has a unique solution, which can be calculated by the following equation:

$$\phi_i(f,x) = \sum_{z' \subseteq x'} \frac{|z'|!(M-|z'|-1)!}{M!} \left[f_x(z') - f_x(z' \backslash i) \right] \tag{26}$$

$$f(x') = f(h_x(z')) = E[f(z)|Z_S] \tag{27}$$

where $|z'|$ is the number of non-empty subsets z' of features used in the model; S is the index of the subsets z'. The Shapley contribution value of each input feature is calculated separately for each sample point in the sample set, which yields the contribution distribution of each input feature.

Suppose a feature has a positive Shapley value. In this case, the feature positively contributes to the model's predictive output (e.g., increasing the predicted outcome or probability). Conversely, if a feature's Shapley value is negative, it indicates that it is reducing or inhibiting a particular prediction. Therefore, it can be understood that the larger the absolute value of a feature's Shapley value (regardless of its sign), the more significant its contribution to the model's predictions.

3. Results

3.1. Estimated Evapotranspiration Maps

3.1.1. Different Time Scale of Evapotranspiration Maps

Using the above method, a total of 182 images from 1988 to 2019 were obtained, and ET was calculated for those dates. Due to space limitations, only the results for 2019 are presented here (Figure 6). As shown in Figure 6, daily ET in June, July, and August 2019 reached approximately 10 mm, while in April, it was around 6 mm. In September and October, daily ET generally remained below 5 mm. During the non-freezing period, the regional average ET (Figure 7) ranges mostly between 200 mm and 600 mm.

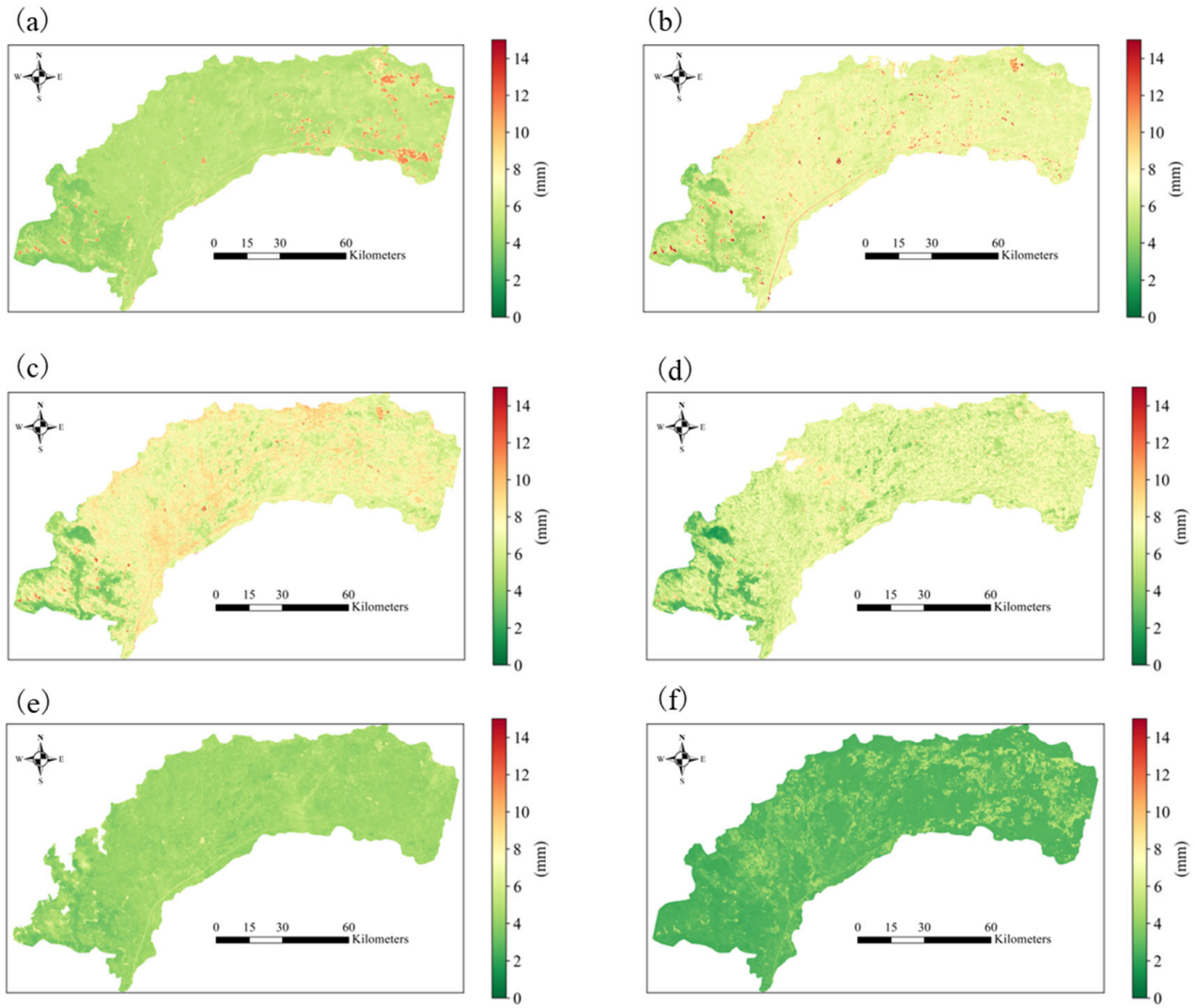

Figure 6. Daily ET map for 2019: (**a**) 21 April, (**b**) 8 June, (**c**) 10 July, (**d**) 27 August, (**e**) 28 September, (**f**) 30 October.

3.1.2. Validation of Evapotranspiration Estimates

The daily ET calculated based on the daily-scale water balance model was compared with the result by the remote sensing method SEBS. As shown in Figure 8, the coefficient of determination (R^2) was 0.78, and the root mean square error (RMSE) was 0.91 mm/day. There are a total of six cloud-free Landsat imageries available at Hetao during the non-freezing season of 2019, which are 21 April, 8 June, 10 July, 27 August, 28 September, and 30 October. As a result, Figure 8 shows twelve validation data points calculated based on the six daily ET maps (Figure 6) at two sites (Figure 3a) using the water balance model. The result shows an R^2 of 0.78 and RMSE of 0.91 for the SEBS predicted ET, indicating high accuracy of the ET estimation.

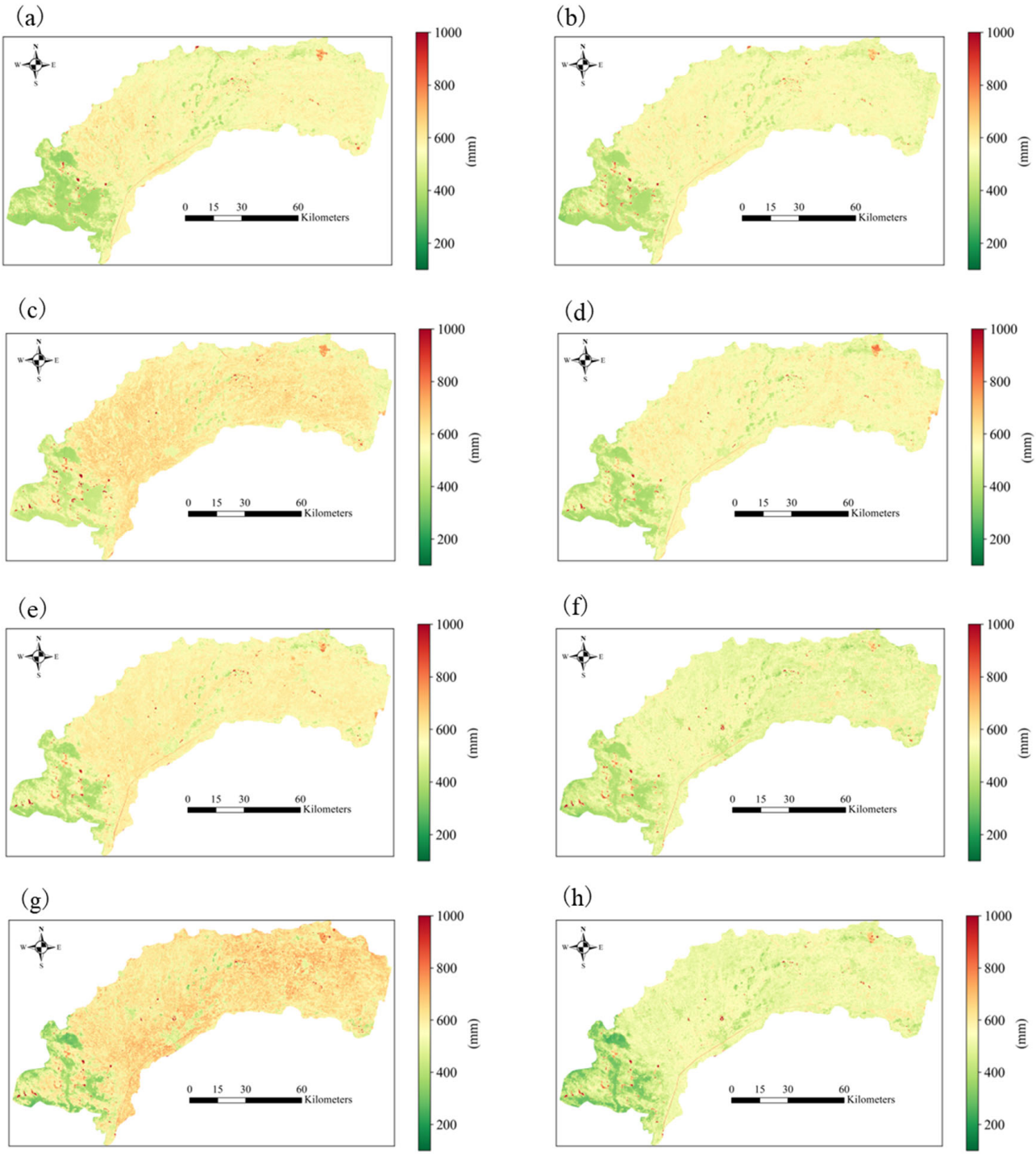

Figure 7. Non-freezing period ET inversion values from 1988 to 2019: (**a**) 1988, (**b**) 1993, (**c**) 1998, (**d**) 2006, (**e**) 2011, (**f**) 2016, (**g**) 2018, (**h**) 2019.

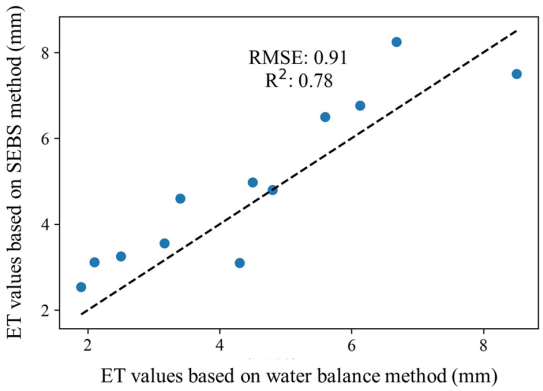

Figure 8. Scatterplot of ET estimated from field-scale water balance and remote sensing- based SEBS.

3.2. Factors Affecting Evapotranspiration in Abandoned Saline Farmland

3.2.1. Degree of Salinization

From the scatter density plot of SI and ET (Figure 9), it can be observed that the annual average SI values of abandoned saline farmland patches are mostly concentrated around 0.2, indicating that most abandoned saline farmland is moderately or highly salinized. The ET of abandoned saline farmland patches was primarily concentrated between 400 mm and 500 mm in 1990, 350 mm and 450 mm in 1999, 400 mm and 500 mm in 2010, and 340 mm and 430 mm in 2019. The Pearson correlation coefficients (r) in Figure 9 indicate a negative relationship between ET and SI across all years, suggesting that higher salinization levels correspond to lower evapotranspiration. The correlation strengthened from 1990 (r = −0.46) to 2010 (r = −0.7), implying an increasing impact of salinization on ET, likely due to prolonged salt accumulation and vegetation degradation. However, in 2019 (r = −0.45), the correlation weakened, suggesting potential ecological recovery, improved water management, or climate variations mitigating the effects of salinization on ET.

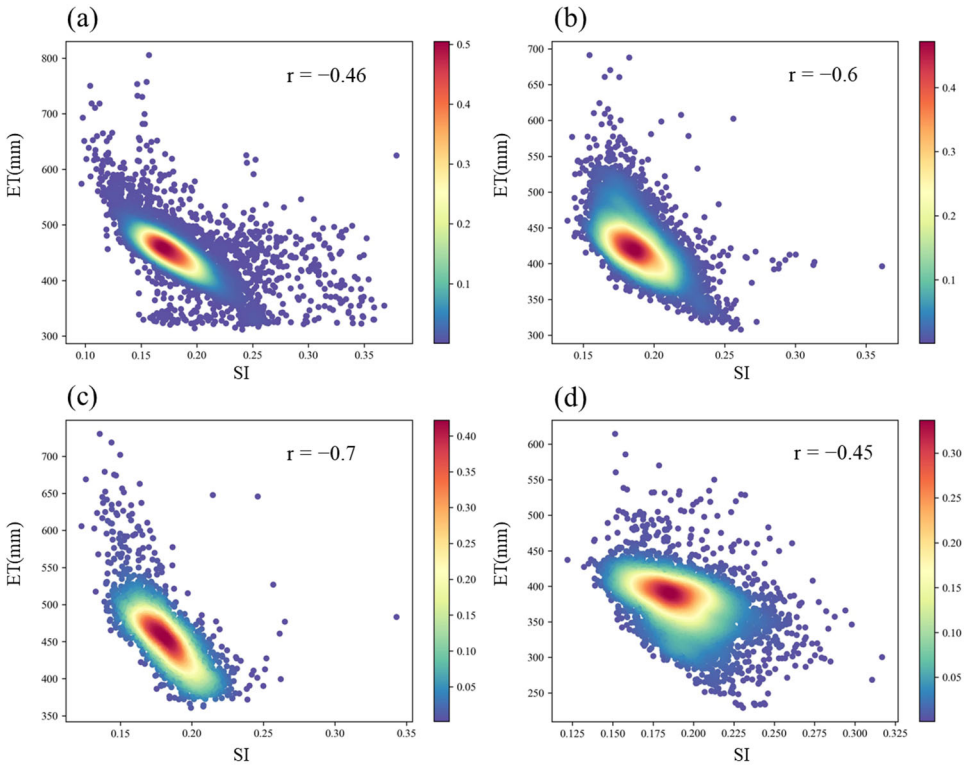

Figure 9. Scatter density plots of ET versus SI for abandoned saline farmland patches in Hetao in (**a**) 1990, (**b**) 1999, (**c**) 2010, and (**d**) 2019.

3.2.2. Salt-Tolerant Vegetation Coverage

From the scatter density plot of NDVI and ET of abandoned saline farmland patches (Figure 10), it can be observed that the NDVI values of abandoned saline farmland patches were primarily concentrated between 0.07 and 0.18 in 1990, 0.06 and 0.15 in 1999, 0.08 and 0.16 in 2010, and 0.10 and 0.22 in 2019. Over the years, there has been an increasing trend in the NDVI values of saline farmland patches. The correlation remained relatively weak in 1990 (r = 0.27) and 1999 (r = 0.26), slightly weakened in 2010 (r = 0.1), and became stronger in 2019 (r = 0.4). Additionally, the NDVI of saline farmland patches is generally positively correlated with ET, indicating that increasing vegetation cover can enhance the ET of abandoned saline farmland patches, thereby improving their dry drainage capacity.

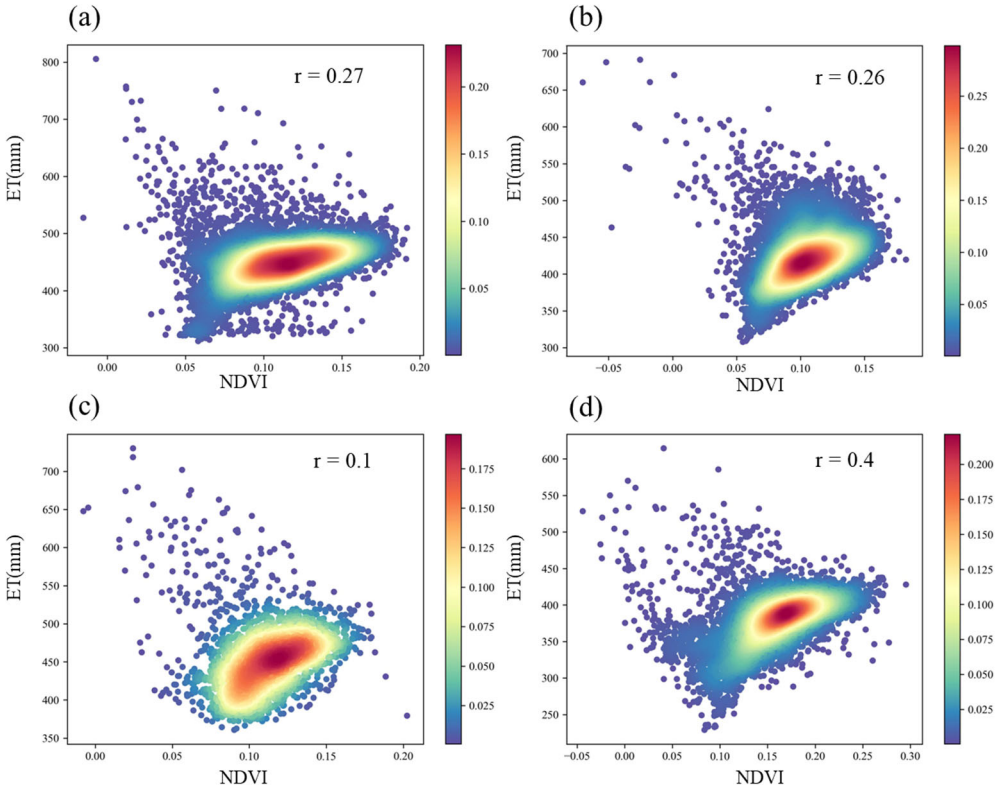

Figure 10. Scatter density plots of ET versus NDVI for abandoned saline farmland patches in Hetao in (**a**) 1990, (**b**) 1999, (**c**) 2010, and (**d**) 2019.

3.2.3. Influence of the Groundwater Table Depth

An analysis was conducted using the 2019 ET results of abandoned saline farmland patches, combined with the average GWTD of abandoned saline farmland patches during the non-freezing period of 2019. As shown in Figure 11, the GWTD of abandoned saline farmland during the non-freezing period spans a wide range, from 1.6 m to 3.0 m, with the majority concentrated between 1.6 m and 2.2 m. Additionally, r is −0.46 in Figure 11 indicates a moderate negative correlation between ET and GWTD in abandoned saline farmland patches. This suggests that as GWTD increases, ET tends to decrease, likely due to reduced capillary water supply to the surface, limiting ET.

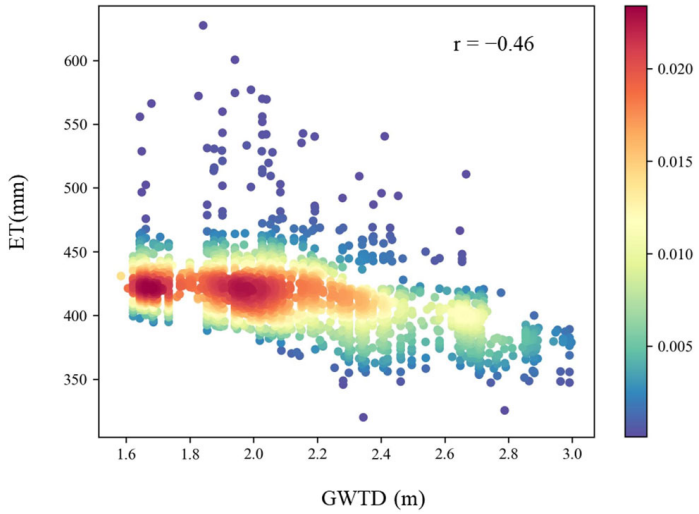

Figure 11. Scatter density plot of annual average groundwater depth (m) and ET (mm) for abandoned saline farmland patches in 2019.

3.2.4. The Area of Abandoned Saline Agricultural Land

The number of abandoned saline farmland (patches) in the Hetao Irrigation District decreased from 9719 in 1988 to 6153 in 2019, indicating a general decline (Figure 12a). After 2010, it shows a plateau in the number of patches, which could be the result of the failure of attempts to reclaim and improve some of the abandoned saline farmland patches. Due to ineffective outcomes or high costs, these reclaimed fields were eventually left uncultivated again. This phenomenon is closely related to the management of water resources in agriculture and the control of salinity in agricultural land.

Among many patches, each one differs in size. For instance, if we look at the 2019 abandoned saline farmland patches and categorize them by their area (Figure 12b), we can see that the majority of these patches (i.e., 90%) fall within the size range of 0 to 5 hectares. This suggests that abandoned saline farmland is predominantly found in a fragmented state within agricultural areas.

Figure 13 illustrates the ET distribution of pixels within abandoned saline farmland patches from 1990 to 2019. The ET of abandoned saline farmlands generally ranges between 200 mm and 600 mm. Notably, in 2001 and 2002, ET was lower due to drought conditions. It can also be observed that the variance in the distribution of abandoned saline farmland ET shows an increasing trend. This is attributed to the progress of desalinization in the Hetao region, which has led to reduced soil salinity in more abandoned saline farmlands. The growth or cultivation of salt-tolerant plants on abandoned saline farmlands has further contributed to the increasing variability in averaged ET across the abandoned saline farmland patches.

Figure 14 illustrates the relationship between abandoned saline farmland area and non-freezing season ET for the years 1990, 1999, 2010, and 2019. The ET is mostly concentrated between 200 mm and 600 mm for abandoned saline farmlands across different area intervals. Due to sufficient lateral groundwater recharge, these smaller abandoned saline farmlands may generate higher ET values. However, variations between years are noticeable, primarily influenced by meteorological factors.

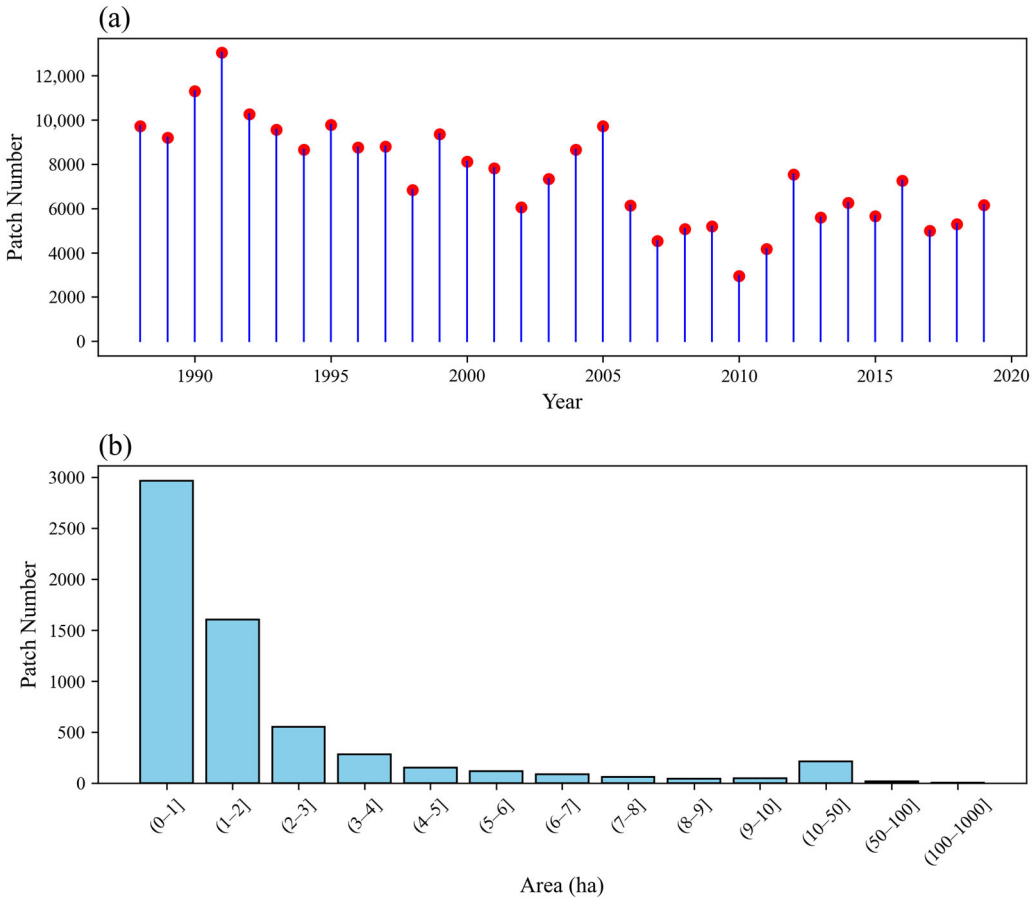

Figure 12. Number of patches in 1988–2019 (**a**), number distribution of abandoned saline farmland (patches) in 2019 (**b**).

Abandoned saline farmlands with areas exceeding 100 hectares generally show lower ET. This could be attributed to higher salinization levels and deeper groundwater tables in larger patches. Due to their extensive size, irrigation in surrounding farmland has minimal impact on altering the overall groundwater table. In contrast, smaller abandoned saline farmland patches with narrower diameters are more susceptible to surrounding farmland irrigation, which can significantly raise their groundwater table. As a result, smaller abandoned saline farmland patches tend to perform better as dry drainage systems for salt removal.

Additionally, abandoned saline farmland of the same size may exhibit differences in ET potential due to various factors, such as salinization levels, vegetation coverage, and groundwater table depth, which collectively influence their ET dynamics.

3.2.5. Spatial Distribution

For the Hetao Irrigation District, the AI was calculated for five landscape units (Figure 4), with the locations of these five units (Figure 3a). As shown in Figure 15, ET reaches its maximum value when the AI is approximately 70% across the five landscape units. However, since ET may also be influenced by other factors, such as groundwater table depth and vegetation conditions within the landscape units, a direct correlation between aggregation and ET cannot be established.

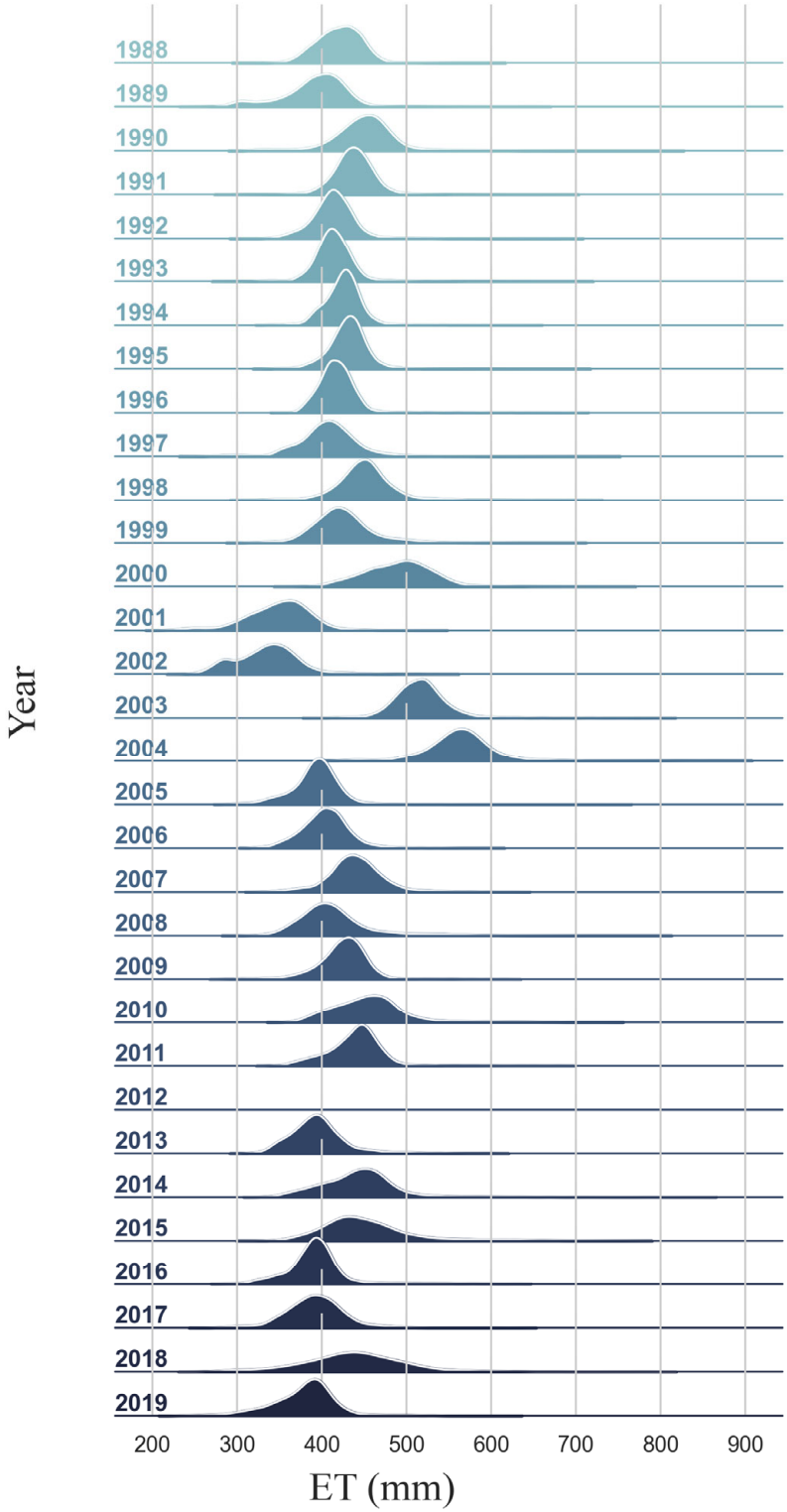

Figure 13. Distribution of averaged ET (mm) over multiple years (1988–2011, 2013–2019) for different abandoned saline area patches.

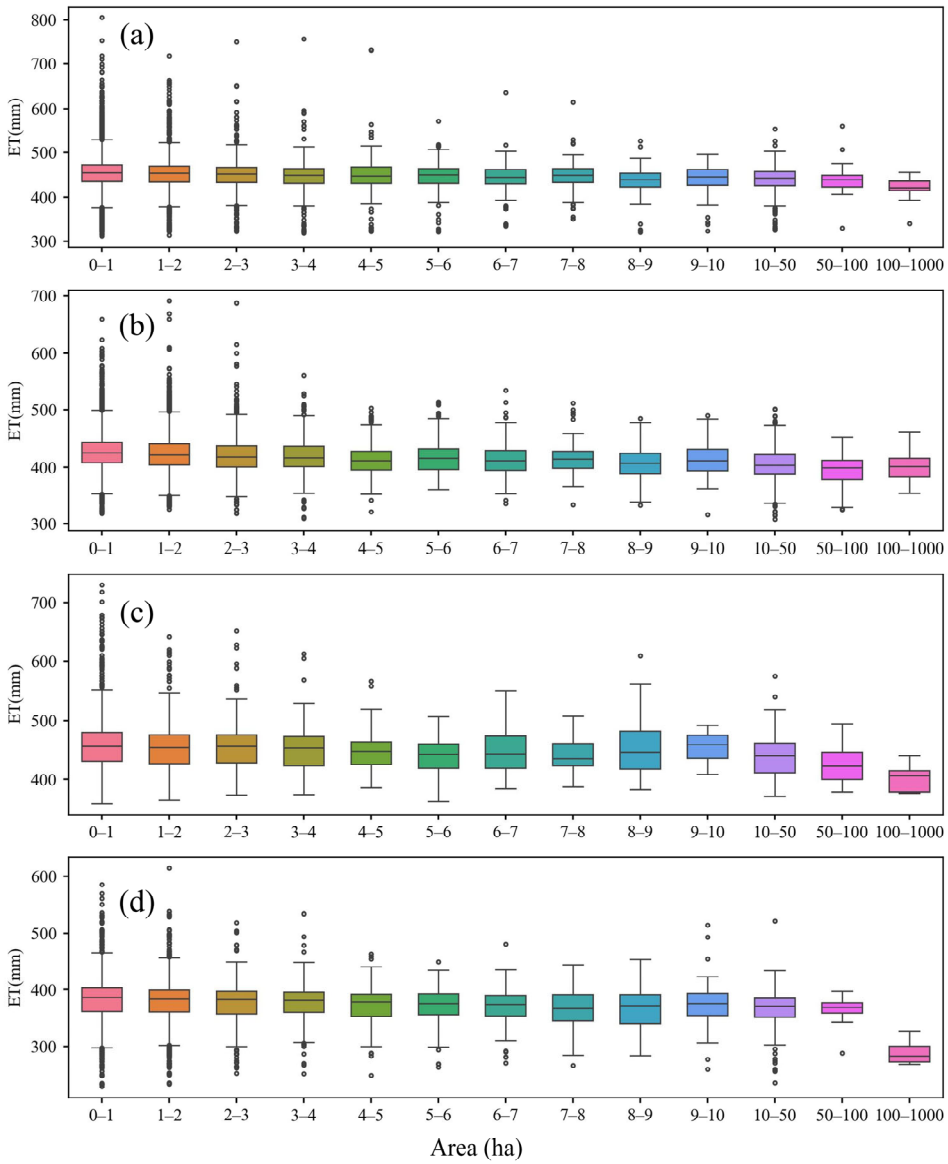

Figure 14. Non-freezing season ET (mm) for different area ranges of abandoned saline farmland in (**a**) 1990, (**b**) 1999, (**c**) 2010, and (**d**) 2019. The values of the independent variable use left-closed and right-open intervals.

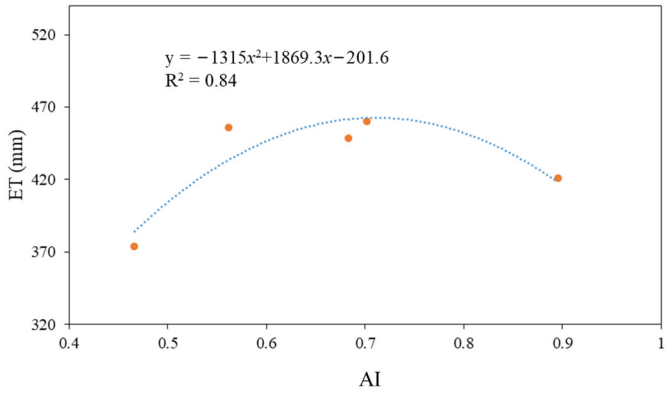

Figure 15. The relationship between AI and ET is based on five landscape cases in the Hetao Irrigation District. The blue dashed line shows the quadratic regression fit.

3.3. Importance of Features in Evapotranspiration in Abandoned Saline Farmland

The correlation matrix of ET in abandoned saline farmland with GWTD, AI, NDVI, SI, and the surface area of abandoned saline farmland is shown in the following table (Table 1). According to the table, ET has a slightly negative correlation with GWTD (r = −0.121), suggesting an increase in groundwater depth could slightly reduce ET. The relationship with the AI of abandoned saline farmland is also slightly negative (r = −0.123), indicating that an increase in aggregation could slightly reduce ET. In contrast, ET shows a stronger positive correlation with the NDVI (r = 0.218), meaning increasing vegetation density could increase ET. The relationship between ET and the SI is weakly negative (r = −0.098), suggesting that an increase in salinity could slightly reduce ET. Finally, the relationship between ET and the surface area of abandoned saline farmland is slightly negative (r = −0.096), indicating that an increase in the area could slightly reduce ET. These data reveal the complex relationships between ET in abandoned saline farmland and several environmental factors, with the positive correlation between NDVI and ET being the most significant.

Table 1. Pearson correlation coefficients between different factors with ET in abandoned saline farmland.

	ET	GWTD	AI	NDVI	SI	Area
ET	1.000	−0.121 ***	−0.123 ***	0.218 ***	−0.098 ***	−0.096 ***
GWTD	−0.121 ***	1.000	−0.012	0.015	−0.069 ***	−0.049 *
AI	−0.123 ***	−0.012	1.000	−0.122 ***	0.280 ***	0.218 ***
NDVI	0.218 ***	0.015	−0.122 ***	1.000	0.043 *	−0.097 ***
SI	−0.098 ***	−0.069 ***	0.280 ***	0.043 *	1.000	0.156 ***
Area	−0.096 ***	−0.049 *	0.218 ***	−0.097 ***	0.156 ***	1.000

Note: Statistical significance is indicated with a p-value where *** $p < 0.001$ (highly significant), * $0.01 \leq p < 0.05$ (moderately significant), and no star $p \geq 0.05$ (not significant).

Figure 16 shows the importance of the indices calculated using the Lasso multivariate linear regression and those calculated using the Random Forest regression. The ranking of the importance of the features is consistent for both methods and for all the features, with NDVI being the most important, followed by GWTD, and the influence of the surface area of abandoned saline farmland being the weakest. The differences in the importance of each feature obtained by Lasso regression are smaller. This is because Lasso regression is a linear model and does not capture the high-dimensional interactions between features. In contrast, Random Forest, which is a nonlinear model, includes the high-dimensional interactions between features in its calculation of feature importance. However, both methods only provide a consolidated importance index and cannot determine the uncertainty in the importance of each feature.

In contrast, feature importance analysis based on the Shapley method can determine the importance of features for individual sample points, thus allowing the determination of the importance distribution of each input feature. The Shapley feature importance analysis results using the Lasso multivariate regression model and the Random Forest (RF) model are shown in Figures 17 and 18, respectively.

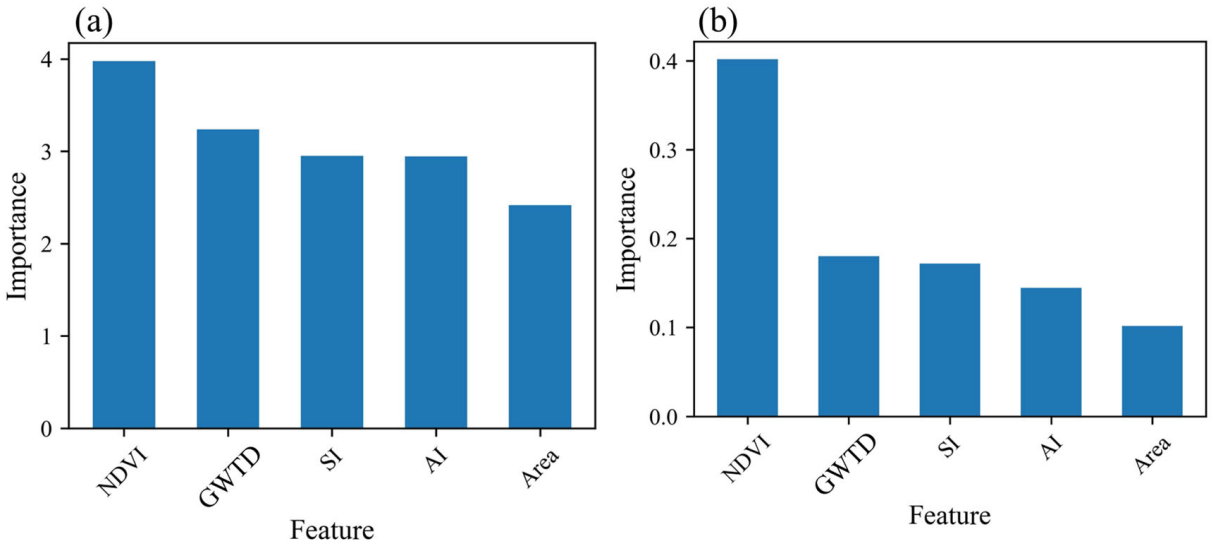

Figure 16. Feature importance analysis based on (**a**) Lasso multivariate linear regression and (**b**) Random Forest regression.

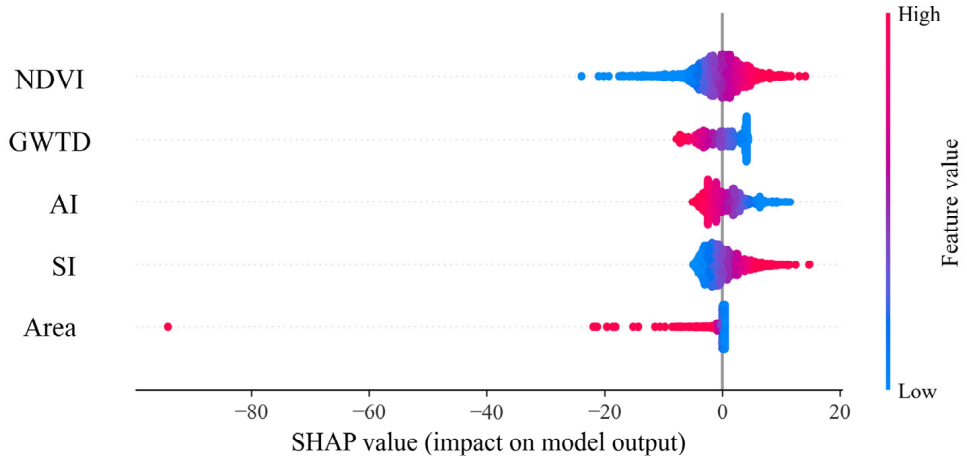

Figure 17. SHAP feature importance for the Lasso multivariate regression model.

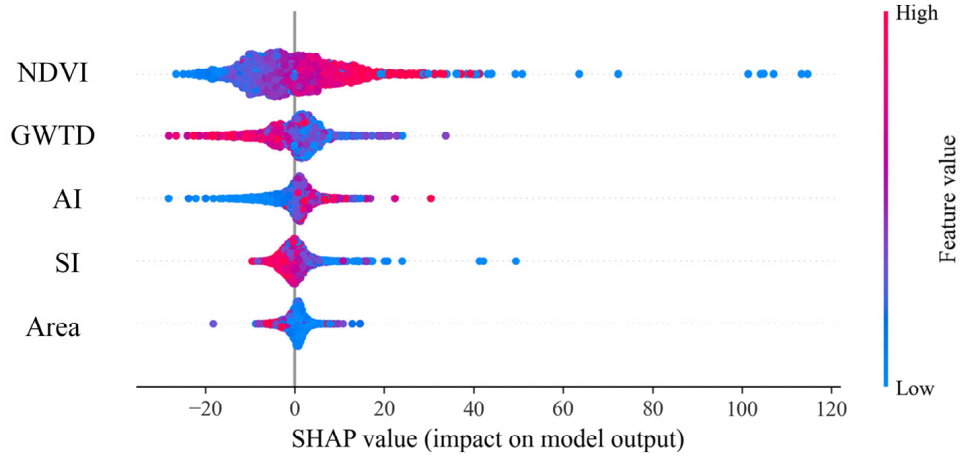

Figure 18. SHAP feature importance for the Random Forest (RF) model.

According to Figures 17 and 18, the distribution of Shapley feature importance generated by Lasso shows substantial irregularities except for NDVI, suggesting that linear models may not capture high-dimensional interactions between variables (features). The

distribution of Shapley feature importance generated by RF is more consistent with a Gaussian distribution, suggesting a highly nonlinear relationship between abandoned saline farmland ET and various features and that RF can explain some of this nonlinearity. Groundwater depth is the second most important feature after NDVI. This is because the crop transpiration process requires the roots to take up water from the soil in the root zone, and groundwater, which replenishes the unsaturated soil moisture by capillary rise, is an essential source of crop water uptake. The AI of abandoned saline farmland is the third most important feature affecting ET, as the distribution of different landscapes can affect groundwater levels and microclimates, indirectly affecting ET. For example, if the AI of abandoned saline farmland is high, groundwater levels will drop, indirectly reducing ET. The area of abandoned saline farmland does not significantly influence the average ET of these abandoned saline farmland, possible reasons being: (1) training sample imbalance, with a lack of samples from large abandoned saline farmlands; (2) substantial spatial variability in the study area; (3) groundwater levels in abandoned saline farmlands were below the critical depth, where groundwater could not produce capillary rise, leading to ET being mainly controlled by rainfall.

4. Discussion

The results reveal a complex interplay between salinization levels, vegetation patterns, and spatial configurations in shaping ET dynamics in abandoned saline farmland. Increased soil salinization was found to be negatively correlated with ET, as higher salinity levels reduce soil hydraulic conductivity through compaction and increased albedo, reducing the energy available for latent heat flux [50]. These results are consistent with previous studies that highlight the inhibitory effects of salinity on water evaporation and plant transpiration. On the other hand, vegetation greenness, represented by NDVI, showed a significant positive correlation with ET, highlighting the role of salt-tolerant vegetation in enhancing ET. This finding corroborates the work of Glenn [51], who reported similar trends in saline ecosystems. The ability of salt-tolerant vegetation to enhance the dry drainage function of saline farmlands is critical for their ecological and hydrological management. Additionally, the spatial configuration of abandoned saline farmland, as indicated by AI, was shown to indirectly influence ET by altering groundwater exchange and microclimatic conditions. Patches with higher aggregation generally exhibited lower ET values, likely due to reduced edge effects and limited groundwater recharge from surrounding areas. Conversely, smaller, fragmented patches exhibited higher ET variability, driven by lateral groundwater recharge from adjacent farmland, which has implications for the effectiveness of abandoned saline farmland as a dry drainage system [7]. These results emphasize the importance of landscape-scale planning in the management of abandoned saline farmlands.

Forman [52] introduced a landscape ecological planning pattern known as “combining concentration and dispersion”, which is widely regarded as the most ecologically optimal landscape pattern. This pattern encompasses seven key landscape ecological attributes, including large natural vegetation patches for water conservation and the support of crucial species, a mix of patch sizes to enhance both overall landscape diversity and local diversity, consideration of risk dispersion during disturbances, preservation of genetic diversity, reduction in boundary resistance through interlocking zones, small natural vegetation patches serving as temporary habitats or refuges, and the incorporation of corridors for species dispersion and the flow of matter and energy. We applied the concept of “combining concentration and dispersion” to saline agricultural land and abandoned saline farmland and found that the spatial distribution of saline patches in the landscape influenced ET processes. Using Landsat imagery to elucidate vegetation greenness, land surface temperature, and land cover, we observed that larger, aggregated saline patches

had higher surface temperatures and lower ET rates, possibly due to increased surface albedo [53] and reduced energy available for latent heat flux. Conversely, smaller, dispersed saline patches often exhibited lower surface temperatures and higher ET rates, possibly due to increased edge effects and enhanced energy exchange between saline and non-saline areas. These results suggest that landscape patterns significantly influence microclimatic conditions and hydrological processes within saline regions. Strategic management of the size and distribution of abandoned saline farmlands can help optimize water use efficiency, mitigate salinity impacts and enhance ecosystem resilience.

Accurately quantifying soil salinity is crucial for understanding its impact on ET and agricultural productivity. Traditional methods of measuring soil salinity, such as electrical conductivity, often require laborious sampling and laboratory analysis. However, Hien [54] demonstrates the potential of Fourier transform infrared spectroscopy (FTIR) as a rapid and non-destructive method for estimating soil salinity. By identifying specific spectral regions sensitive to salt content, this technique offers a promising avenue for developing remote sensing-based salinity maps [55]. Further research is needed to explore the applicability of FTIR to regional scales with a wider range of soil types and salinity levels. Additionally, combining FTIR with other remote sensing methods and indices [56], including thermal infrared [57], could enhance the accuracy and spatial resolution of salinity mapping, ultimately improving our ability to monitor and manage salt-affected soils and patches of abandoned saline farmland.

In this study, a control variate method was used to investigate the correlation between selected factors and ET. By aggregating ET and the investigated factors to the non-freezing period scale and focusing on the Yichang subdistrict, we assumed that meteorological conditions were consistent across all sampling sites, rendering the actual ET of the sampling sites invariant to the reference ET_0. Although the correlations between the investigated factors and ET were relatively low, the high significance levels for all factors can be attributed to the large number of samples analyzed (2458 abandoned saline farmland patches). However, we acknowledge that the factors investigated may not account for all potential influences, such as heterogeneous soil moisture levels, even in areas with similar meteorological conditions. This limitation highlights the need for future research to comprehensively investigate additional factors that may influence ET in saline environments. Addressing these gaps will improve the robustness of ET modeling and its application to saline farmland management.

5. Conclusions

In addition to meteorological factors, the ET in abandoned saline farmland is also affected by several other factors, such as the depth of groundwater in abandoned saline farmland, the coverage of salt-tolerant vegetation, the degree of salinization, the spatial arrangement of abandoned saline farmland, and the area size of abandoned saline farmland patches. The existing literature does not analyze the effects of salinization levels, vegetation cover, and spatial layout of abandoned saline farmland on ET. This study addressed this gap by investigating the influence of the above-mentioned factors on ET of abandoned saline farmland in the Hetao Irrigation District. This research employs the SEBS energy balance model to estimate ET in the Hetao Irrigation District remotely. Combined with the spatial information of abandoned saline farmland [5], the averaged ET of abandoned saline farmland patches was obtained. Subsequently, Shapley, Lasso, and Random Forest feature importance analysis methods were used to evaluate the impacts of factors such as vegetation coverage, soil salinity, groundwater table depth, and landscape indices on the patch-level ET of abandoned saline farmland. Our findings reveal that the ET of abandoned saline farmland is influenced not only by common factors such as vegetation greenness and groundwater table depth but also significantly by soil salinity and the landscape aggre-

gation of abandoned saline farmland. The fragmented distribution of abandoned saline farmland within farmland leads to significant variability in ET. For smaller abandoned saline farmland, lateral groundwater recharge results in higher ET variability. Conversely, larger abandoned saline farmland exhibits more stable ET, enabling them to perform their dry drainage function better. Abiotic factors such as shallower groundwater table depth, lower soil salinity, and lower abandoned saline farmland aggregation positively influence ET. The results from the Random Forest model reveal highly nonlinear relationships between ET and these factors. Among them, groundwater recharge to the unsaturated zone is identified as a key driver of ET, while abandoned saline farmland aggregation influences ET indirectly by affecting groundwater exchange and regional microclimatic conditions.

Supplementary Materials: The following supporting information can be downloaded at: https://www.mdpi.com/article/10.3390/land14020283/s1, Figure S1: Field Photos of Experimental Sites; Table S1: Date Information of Downloaded Landsat Images.

Author Contributions: Conceptualization, L.Z.; methodology, L.Z. and Q.Y.; software, L.Z. and Q.Y.; validation, L.Z.; formal analysis, L.Z. and Q.Y.; investigation, L.Z., J.M., H.Z., Z.Y. and Y.L.; resources, J.W. and A.G.; data curation, L.Z. and Q.Y.; writing—original draft preparation, L.Z. and Q.Y.; writing—review and editing, J.W. and A.G.; visualization, L.Z.; supervision, J.W. and A.G.; project administration, J.W. and A.G.; funding acquisition, J.W. and A.G. All authors have read and agreed to the published version of the manuscript.

Funding: This research was funded by the National Science Foundation of China (Grants No. 52379047, 52209067) and the KU Leuven internal funding STG/21/027.

Data Availability Statement: The data presented in this study are available on request from the corresponding author due to restrictions imposed by the funding organization.

Acknowledgments: We are grateful to the editor and anonymous reviewers for their valuable comments and others who contributed to this paper.

Conflicts of Interest: The authors declare no conflicts of interest.

References

1. Thomas, D.S.G.; Middleton, N.J. Salinization: New Perspectives on a Major Desertification Issue. *J. Arid Environ.* **1993**, *24*, 95–105. [CrossRef]
2. Aslam, M.; Prathapar, S.A.; Aslam, M.; Prathapar, S.A. *Strategies to Mitigate Secondary Salinization in the Indus Basin of Pakistan: A Selective Review*; International Water Management Institute (IWMI): Colombo, Sri Lanka, 2006.
3. Kitamura, Y.; Yano, T.; Honna, T.; Yamamoto, S.; Inosako, K. Causes of Farmland Salinization and Remedial Measures in the Aral Sea Basin—Research on Water Management to Prevent Secondary Salinization in Rice-Based Cropping System in Arid Land. *Agric. Water Manag.* **2006**, *85*, 1–14. [CrossRef]
4. Yang, H.; Zhang, F.; Chen, Y.; Xu, T.; Cheng, Z.; Liang, J. Assessment of Reclamation Treatments of Abandoned Farmland in an Arid Region of China. *Sustainability* **2016**, *8*, 1183. [CrossRef]
5. Zhao, L.; Yang, Q.; Zhao, Q.; Wu, J. Assessing the Long-Term Evolution of Abandoned Salinized Farmland via Temporal Remote Sensing Data. *Remote Sens.* **2021**, *13*, 4057. [CrossRef]
6. Romero-Díaz, A.; Pérez-Morales, A.; Marín-Sanleandro, P. Prevalence, Causes, and Consequences of Agricultural Land Abandonment: A Case Study in the Region of Murcia, Spain. *CATENA* **2024**, *241*, 108071. [CrossRef]
7. Konukcu, F.; Gowing, J.W.; Rose, D.A. Dry Drainage: A Sustainable Solution to Waterlogging and Salinity Problems in Irrigation Areas? *Agric. Water Manag.* **2006**, *83*, 1–12. [CrossRef]
8. Wu, J.; Zhao, L.; Huang, J.; Yang, J.; Vincent, B.; Bouarfa, S.; Vidal, A. On the Effectiveness of Dry Drainage in Soil Salinity Control. *Sci. China Ser. E-Technol. Sci.* **2009**, *52*, 3328–3334. [CrossRef]
9. Yu, B.; Jiang, L.; Shang, S. Dry Drainage Effect of Hetao Irrigation District Based on Remote Sensing Evapotranspiration. *Trans. Chin. Soc. Agric. Eng.* **2016**, *32*, 1–8.
10. Khouri, N. Potential of Dry Drainage for Controlling Soil Salinity. *Can. J. Civ. Eng.* **1998**, *25*, 195–205. [CrossRef]
11. Gowing, J.W.; Wyseure, G.C.L. Dry-Drainage a Sustainable and Cost-Effective Solution to Waterlogging and Salinisation. Proceedings of the 5th International Drainage Workshop, Lahore, Pakistan, 8–15 February 1992; Volume 3, pp. 6–26.

12. Raza, A.; Hu, Y.; Acharki, S.; Buttar, N.A.; Ray, R.L.; Khaliq, A.; Zubair, N.; Zubair, M.; Syed, N.R.; Elbeltagi, A. Evapotranspiration Importance in Water Resources Management Through Cutting-Edge Approaches of Remote Sensing and Machine Learning Algorithms. In *Surface and Groundwater Resources Development and Management in Semi-arid Region: Strategies and Solutions for Sustainable Water Management*; Pande, C.B., Kumar, M., Kushwaha, N.L., Eds.; Springer International Publishing: Cham, Switzerland, 2023; pp. 1–20. ISBN 978-3-031-29394-8.
13. Pereira, L.S.; Allen, R.G.; Smith, M.; Raes, D. Crop Evapotranspiration Estimation with FAO56: Past and Future. *Agric. Water Manag.* **2015**, *147*, 4–20. [CrossRef]
14. Pereira, L.S.; Perrier, A.; Allen, R.G.; Alves, I. Evapotranspiration: Concepts and Future Trends. *J. Irrig. Drain Eng.* **1999**, *125*, 45–51. [CrossRef]
15. Van Wijk, W.R.; De Vries, D.A. Evapotranspiration. *Neth. J. Agric. Sci.* **1954**, *2*, 105–119.
16. Tanner, C.B. Measurement of Evapotranspiration. In *Agronomy Monographs*; Hagan, R.M., Haise, H.R., Edminster, T.W., Eds.; American Society of Agronomy: Madison, WI, USA, 2015; pp. 534–574. ISBN 978-0-89118-206-1.
17. Rijtema, P.E. An Analysis of Actual Evapotranspiration. Ph.D. Thesis, Pudoc, San Vicente, Philippines, 1965.
18. Mondal, S.; Mishra, A. Quantifying the Precipitation, Evapotranspiration, and Soil Moisture Network's Interaction Over Global Land Surface Hydrological Cycle. *Water Resour. Res.* **2024**, *60*, e2023WR034861. [CrossRef]
19. Gowda, P.H.; Chavez, J.L.; Colaizzi, P.D.; Evett, S.R.; Howell, T.A.; Tolk, J.A. ET Mapping for Agricultural Water Management: Present Status and Challenges. *Irrig Sci* **2008**, *26*, 223–237. [CrossRef]
20. Jiang, L.; Islam, S. A Methodology for Estimation of Surface Evapotranspiration over Large Areas Using Remote Sensing Observations. *Geophys. Res. Lett.* **1999**, *26*, 2773–2776. [CrossRef]
21. Zhang, K.; Kimball, J.S.; Running, S.W. A Review of Remote Sensing Based Actual Evapotranspiration Estimation. *WIREs Water* **2016**, *3*, 834–853. [CrossRef]
22. Taheri, M.; Mohammadian, A.; Ganji, F.; Bigdeli, M.; Nasseri, M. Energy-Based Approaches in Estimating Actual Evapotranspiration Focusing on Land Surface Temperature: A Review of Methods, Concepts, and Challenges. *Energies* **2022**, *15*, 1264. [CrossRef]
23. Senay, G.B.; Leake, S.; Nagler, P.L.; Artan, G.; Dickinson, J.; Cordova, J.T.; Glenn, E.P. Estimating Basin Scale Evapotranspiration (ET) by Water Balance and Remote Sensing Methods. *Hydrol. Process.* **2011**, *25*, 4037–4049. [CrossRef]
24. Liu, J.; Chen, J.M.; Cihlar, J. Mapping Evapotranspiration Based on Remote Sensing: An Application to Canada's Landmass. *Water Resour. Res.* **2003**, *39*, 2002WR001680. [CrossRef]
25. Wright, J.L. New Evapotranspiration Crop Coefficients. *J. Irrig. Drain. Div.* **1982**, *108*, 57–74. [CrossRef]
26. Monteith, J.L. Evaporation and Environment. *Symp. Soc. Exp. Biol.* **1965**, *19*, 205–234. [PubMed]
27. Chen, J.M.; Liu, J. Evolution of Evapotranspiration Models Using Thermal and Shortwave Remote Sensing Data. *Remote Sens. Environ.* **2020**, *237*, 111594. [CrossRef]
28. Glenn, E.P.; Neale, C.M.U.; Hunsaker, D.J.; Nagler, P.L. Vegetation Index-Based Crop Coefficients to Estimate Evapotranspiration by Remote Sensing in Agricultural and Natural Ecosystems. *Hydrol. Process.* **2011**, *25*, 4050–4062. [CrossRef]
29. Hu, X.; Shi, L.; Lin, L.; Zhang, B.; Zha, Y. Optical-Based and Thermal-Based Surface Conductance and Actual Evapotranspiration Estimation, an Evaluation Study in the North China Plain. *Agric. For. Meteorol.* **2018**, *263*, 449–464. [CrossRef]
30. Jarvis, P.G.; Monteith, J.L.; Weatherley, P.E. The Interpretation of the Variations in Leaf Water Potential and Stomatal Conductance Found in Canopies in the Field. *Philos. Trans. R. Soc. Lond. B Biol. Sci.* **1997**, *273*, 593–610. [CrossRef]
31. Meng, C.L.; Li, Z.-L.; Zhan, X.; Shi, J.C.; Liu, C.Y. Land Surface Temperature Data Assimilation and Its Impact on Evapotranspiration Estimates from the Common Land Model. *Water Resour. Res.* **2009**, *45*, 2008WR006971. [CrossRef]
32. Xiong, Y.J.; Qiu, G.Y. Estimation of Evapotranspiration Using Remotely Sensed Land Surface Temperature and the Revised Three-Temperature Model. *Int. J. Remote Sens.* **2011**, *32*, 5853–5874. [CrossRef]
33. Jin, Y.; He, R.; Marino, G.; Whiting, M.; Kent, E.; Sanden, B.L.; Culumber, M.; Ferguson, L.; Little, C.; Grattan, S. Spatially Variable Evapotranspiration over Salt Affected Pistachio Orchards Analyzed with Satellite Remote Sensing Estimates. *Agric. For. Meteorol.* **2018**, *262*, 178–191. [CrossRef]
34. Aboelsoud, H.M.; Habib, A.; Engel, B.; Hashem, A.A.; Abou El-Hassan, W.; Govind, A.; Elnashar, A.; Eid, M.; Kheir, A.M. The Combined Impact of Shallow Groundwater and Soil Salinity on Evapotranspiration Using Remote Sensing in an Agricultural Alluvial Setting. *J. Hydrol. Reg. Stud.* **2023**, *47*, 101372. [CrossRef]
35. Lai, Y.; Wu, D.; Zhang, M. Crystallization Deformation of a Saline Soil during Freezing and Thawing Processes. *Appl. Therm. Eng.* **2017**, *120*, 463–473. [CrossRef]
36. Ren, D.; Xu, X.; Engel, B.; Huang, G. Growth Responses of Crops and Natural Vegetation to Irrigation and Water Table Changes in an Agro-Ecosystem of Hetao, Upper Yellow River Basin: Scenario Analysis on Maize, Sunflower, Watermelon and Tamarisk. *Agric. Water Manag.* **2018**, *199*, 93–104. [CrossRef]
37. Gobin, A.; Sallah, A.-H.M.; Curnel, Y.; Delvoye, C.; Weiss, M.; Wellens, J.; Piccard, I.; Planchon, V.; Tychon, B.; Goffart, J.-P.; et al. Crop Phenology Modelling Using Proximal and Satellite Sensor Data. *Remote Sens.* **2023**, *15*, 2090. [CrossRef]

38. Durgun, Y.Ö.; Gobin, A.; Van De Kerchove, R.; Tychon, B. Crop Area Mapping Using 100-m Proba-V Time Series. *Remote Sens.* **2016**, *8*, 585. [CrossRef]
39. Qin, Z.H.; Li, W.J.; Xu, B.; Chen, Z.; Liu, J. The Estimation of Land Surface Emissivity for Landsat TM6. *Remote Sens. Land Resour.* **2004**, *3*, 28–32.
40. Qin, Z.; Karnieli, A.; Berliner, P. A Mono-Window Algorithm for Retrieving Land Surface Temperature from Landsat TM Data and Its Application to the Israel-Egypt Border Region. *Int. J. Remote Sens.* **2001**, *22*, 3719–3746. [CrossRef]
41. Su, Z. The Surface Energy Balance System (SEBS) for Estimation of Turbulent Heat Fluxes. *Hydrol. Earth Syst. Sci.* **2002**, *6*, 85–100. [CrossRef]
42. Tang, R.; Li, Z.-L.; Sun, X. Temporal Upscaling of Instantaneous Evapotranspiration: An Intercomparison of Four Methods Using Eddy Covariance Measurements and MODIS Data. *Remote Sens. Environ.* **2013**, *138*, 102–118. [CrossRef]
43. Liu, Y.; Pereira, L.S.; Fernando, R.M. Fluxes through the Bottom Boundary of the Root Zone in Silty Soils: Parametric Approaches to Estimate Groundwater Contribution and Percolation. *Agric. Water Manag.* **2006**, *84*, 27–40. [CrossRef]
44. Peng, Z.; Guo, H.; Wu, J.; Huang, J. Contribution of Osmotic Potential on Bare Soil Evaporation Rate. *Adv. Water Sci.* **2013**, *24*, 235–242.
45. O'Neill, R.V.; Krummel, J.R.; Gardner, R.H.; Sugihara, G.; Jackson, B.; DeAngelis, D.L.; Milne, B.T.; Turner, M.G.; Zygmunt, B.; Christensen, S.W.; et al. Indices of Landscape Pattern. *Landsc. Ecol* **1988**, *1*, 153–162. [CrossRef]
46. He, H.S.; DeZonia, B.E.; Mladenoff, D.J. An Aggregation Index (AI) to Quantify Spatial Patterns of Landscapes. *Landsc. Ecol.* **2000**, *15*, 591–601. [CrossRef]
47. Tibshirani, R. Regression Shrinkage and Selection via the Lasso. *J. R. Stat. Soc. Ser. B Stat. Methodol.* **1996**, *58*, 267–288. [CrossRef]
48. Breiman, L. Random Forests. *Mach. Learn.* **2001**, *45*, 5–32. [CrossRef]
49. Lundberg, S.M.; Lee, S.-I. A Unified Approach to Interpreting Model Predictions. In *Advances in Neural Information Processing Systems*; Curran Associates, Inc.: New York, NY, USA, 2017; Volume 30.
50. Adeyemo, T.; Kramer, I.; Levy, G.J.; Mau, Y. Salinity and Sodicity Can Cause Hysteresis in Soil Hydraulic Conductivity. *Geoderma* **2022**, *413*, 115765. [CrossRef]
51. Glenn, E.P.; Nagler, P.L.; Huete, A.R. Vegetation Index Methods for Estimating Evapotranspiration by Remote Sensing. *Surv. Geophys.* **2010**, *31*, 531–555. [CrossRef]
52. Forman, R.T.T. Some General Principles of Landscape and Regional Ecology. *Landsc. Ecol.* **1995**, *10*, 133–142. [CrossRef]
53. Zhang, X.; Jiao, Z.; Zhao, C.; Qu, Y.; Liu, Q.; Zhang, H.; Tong, Y.; Wang, C.; Li, S.; Guo, J. Review of Land Surface Albedo: Variance Characteristics, Climate Effect and Management Strategy. *Remote Sens.* **2022**, *14*, 1382. [CrossRef]
54. Hien, L.T.T.; Gobin, A.; Lim, D.T.; Quan, D.T.; Hue, N.T.; Thang, N.N.; Binh, N.T.; Dung, V.T.K.; Linh, P.H. Soil Moisture Influence on the FTIR Spectrum of Salt-Affected Soils. *Remote Sens.* **2022**, *14*, 2380. [CrossRef]
55. Mohamed, S.A.; Metwaly, M.M.; Metwalli, M.R.; AbdelRahman, M.A.; Badreldin, N. Integrating Active and Passive Remote Sensing Data for Mapping Soil Salinity Using Machine Learning and Feature Selection Approaches in Arid Regions. *Remote Sens.* **2023**, *15*, 1751. [CrossRef]
56. AbdelRahman, M.A.; Afifi, A.A.; D'Antonio, P.; Gabr, S.S.; Scopa, A. Detecting and Mapping Salt-Affected Soil with Arid Integrated Indices in Feature Space Using Multi-Temporal Landsat Imagery. *Remote Sens.* **2022**, *14*, 2599. [CrossRef]
57. Tian, F.; Hou, M.; Qiu, Y.; Zhang, T.; Yuan, Y. Salinity Stress Effects on Transpiration and Plant Growth under Different Salinity Soil Levels Based on Thermal Infrared Remote (TIR) Technique. *Geoderma* **2020**, *357*, 113961. [CrossRef]